IEEE Access
Multidisciplinary | Rapid Review | Open Access Journal

Received 2 October 2025, accepted 9 November 2025, date of publication 20 November 2025, date of current version 4 December 2025.

Digital Object Identifier 10.1109/ACCESS.2025.3635391

RESEARCH ARTICLE

Fundamental Limits of Wireless Localization With LoRa Technology

AMIR SHEHNI[1], (Member, IEEE), AHMED ELZANATY[2], (Senior Member, IEEE), FRANCESCO GUIDI[1], (Member, IEEE), ANNA GUERRA[3], (Member, IEEE), GIANNI PASOLINI[3], (Member, IEEE), AND DAVIDE DARDARI[3], (Fellow, IEEE)

[1]National Research Council of Italy (CNR), 40136 Bologna, Italy
[2]5GIC and 6GIC, Institute for Communication Systems (ICS), University of Surrey, GU2 7XH Guildford, U.K.
[3]WiLab, University of Bologna, 40136 Bologna, Italy

Corresponding author: Francesco Guidi (francesco.guidi@cnr.it)

This work was supported in part by the Consiglio Nazionale delle Ricerche-Institute of Electronics, Computer, and Telecommunication Engineering (CNR-IEIIT), Italy, through the project "AMBIENTI RADIO INTELLIGENTI 6G BASATI SU METASUPERFICI–HOLOGRAPHIC RADIO–HOLO"; in part by European Union through Italian National Recovery and Resilience Plan (NRRP) of NextGenerationEU, partnership (Mission 4—Component 2—Investment 1.1) Progetti di Ricerca di Rilevante Interesse Nazionale (PRIN) 2022 (No. 104, 2/2/2022), under Grant CUP J53C24002790006; in part by European Research Council (ERC) through the Project CUE-GO: Contextual Radio Cues for Enhancing Decision Making in Networks of Autonomous Agents, under Grant 101116257; and in part by the Competitive Research Grant (CRG) from King Abdullah University of Science and Technology (KAUST), "Toward IoT Everywhere"; and in part by the UK EPSRC Communications Hub for Empowering Distributed Cloud Computing Applications and Research (CHEDDAR) under Grant EP/X040518/1 and Grant EP/Y037421/1.

ABSTRACT Wireless localization is emerging as a critical service in Internet of Things (IoT) applications, with Long Range (LoRa) technology gaining considerable attention due to its cost-effectiveness and extended-range capabilities. Given these distinctive features, this paper studies LoRa-based localization systems, focusing on the maximum likelihood estimator (MLE) algorithm as a direct localization approach and evaluating fundamental performance limits. Specifically, we derive the Cramér-Rao lower bound (CRLB) to assess localization accuracy, covering both the direct MLE method and time difference of arrival (TDOA) techniques. Numerical results suggest that LoRa signals hold substantial promise for localization, achieving meter-level accuracy without requiring additional infrastructure beyond the existing LoRa network used for communication.

INDEX TERMS LoRa, localization, TDOA, TOA, fundamental limits, Cramér–Rao lower bound (CRLB).

I. INTRODUCTION

Over the past decade, the IoT has attracted significant attention from both academia and industry, driven by the growing need to connect a diverse array of "things" while meeting critical requirements such as low power consumption, long-range communication, and cost-effectiveness [1], [2], [3]. Although traditional technologies, like Zigbee and Bluetooth, have been explored for IoT connectivity, they often fall short in coverage, making them less suitable for long-range applications, particularly in smart city scenarios [4], [5].

To overcome these limitations, the Low-Power Wide-Area Network (LPWAN) technology was introduced to meet IoT communication needs, offering key features such as extended range and low power consumption [6]. Among the various LPWAN options, the Long-Range Wide-Area Network (LoRaWAN) technology, developed by Semtech in 2012, has become particularly prominent [7]. At the physical layer, LoRaWAN employs the LoRa modulation, which is based on the chirp spread spectrum (CSS) modulation. This technique utilizes a larger bandwidth than strictly necessary to enhance the signal's resilience to noise, interference, and jamming attacks [8], [9]. Its unique characteristics, including waveform and spectral properties are discussed in works like [10], [11], [12].

LoRa performance in IoT scenarios is analyzed in [13], and its applications have been explored in various contexts, including multiple-input multiple-output (MIMO) systems [14], reconfigurable intelligent surfaces [15],

The associate editor coordinating the review of this manuscript and approving it for publication was Mohammad S. Khan.

backscatter communications [16], unmanned aerial vehicle (UAV) communications [17], satellite communications [18], and relay networks [19]. Furthermore, joint communication and localization applications are presented in [20], which investigates LoRa-based systems for underground applications, and in [21], where an active tracking model is proposed to detect movements of LoRa transmitters.

Given the critical importance of localization in modern wireless systems [22], [23], [24], [25], [26], [27], [28], particularly in IoT and Industry 4.0 applications, several studies have explored LoRa's potential for this purpose. For instance, [29] and [30] provide a broad analysis of LoRa for localization, discussing its benefits and limitations. Furthermore, [31] demonstrates the feasibility of achieving high localization accuracy in indoors using LoRa. Through experimental data and received signal strength (RSS) measurements, this study shows that LoRa can deliver robust localization accuracy in both line-of-sight (LOS) and non line-of-sight (NLOS) indoor environments.

A research in [32] combines LoRa technology with a fingerprinting approach that uses the constant motion method for data collection. It employs a two-layer Deep Gaussian Process Regression (DGPR) model to address the non-linear nature of signal propagation. A LoRa-based localization system that uses satellite images to generate virtual fingerprints is also proposed in [33]. By integrating commercial LoRa devices with land-cover data, propagation models are refined to create a more realistic representation closely aligned with actual environments.

Then, [34] developed an indoor room-level localization system based on LoRa signal backscattering. This system uses a low-cost LoRa network that, exploiting RSS measurements, achieves effective localization performance when good coverage is available. Machine learning techniques are then applied to enhance results in areas with limited coverage. In [35] the authors investigated LoRa-based localization for GPS-denied emergency scenarios, focusing on its power efficiency using the RSS technique. Then, [36] examined experimental data on RSS for both indoor and outdoor LoRa-based localization, highlighting its accuracy in specific configurations as well as its potential unreliability in noisy urban environments. To address the challenges of using RSS measurements for localization in such conditions, several solutions have been proposed. For example, [37] introduced two algorithms: the first made use of k-means clustering followed by localization calculations, while the second selected the optimal solution based on estimated RSS errors across all potential locations. Building on this work, [38] developed iterative algorithms to more effectively reduce non-Gaussian noise, improving previous models. Then, [39] presented a more advanced study proposing various RSS-based localization algorithms designed to mitigate the effects of Gaussian and non-Gaussian noise in LoRa networks, demonstrating effective performance in both outdoor and large-scale indoor environments. Furthermore, [40] introduced a LoRa-based system capable of localizing multiple targets, employing a single mobile anchor comprised of a LoRa gateway and a typical smartphone to track several IoT devices equipped with LoRa tags. RSS-based localization with LoRa has also been used in aerial applications. For example, a drone-assisted localization system for LoRa IoT networks is presented in [41], demonstrating significant accuracy enhancements achieved by utilizing drones as mobile gateways. Another drone research using LoRa is presented in [42] where it incorporates sensor-derived altitude data and utilizes the Huber loss function in the multilateration optimization process, leading to improved accuracy over traditional RSSI-based methods and demonstrating better scalability with an increasing number of beacons. Lastly, some practical research for LoRa-based localization problems are done in the works like [43] and [44] in which it is proposed a method for boosting the received signal strength on a moving path of LoRa wireless networking without change in digital circuitry or power amplifiers, and the second uses machine learning techniques for antenna design for LoRa location tracking applications.

While RSS-based localization techniques have been extensively explored in LoRa networks, experimental data from the authors in [45] suggest that TDOA can achieve superior accuracy compared to RSS methods. Consequently, TDOA has gained attention in LoRa-based localization systems, leveraging the advantages of large spreading factors (SFs) and dense gateway deployments [30], [46], [47]. Although [48] reports that time-stamping trilateration techniques outperform RSS-based methods at low signal-to-noise ratios (SNRs), challenges arise from narrow-band radio channels and high timestamp granularity. To address these challenges, [49] introduced a two-stage timestamp estimation approach that enhances localization accuracy without the need for signal oversampling. Additionally, [50] examined both iterative and non-iterative TDOA-based algorithms using LoRa devices for localization. Reference [51] further evaluated node tracking performance within a public LoRa network using TDOA.

To the best of our knowledge, prior CRLB analyses in the context of LoRa [49], [52], [53], [54] have either focused on envelope-based signal processing (e.g., time-of-arrival (TOA) estimation, RSSI-based ranging, or correlation-based approaches), or have incorporated phase in the signal model without deriving fundamental limits that explicitly include phase in the Fisher Information Matrix (FIM). Notably, while phase-based CRLB analyses have been deeply investigated in the broader localization literature [55], [56], [57], [58], [59], our contribution lies in adapting this framework to the unique chirp spread spectrum modulation of LoRa. This yields theoretical benchmarks that are directly relevant for LoRa-based systems.

In contrast to existing literature, this paper provides a more comprehensive analysis of wireless localization systems employing LoRa signaling and incorporating both RSS and phase information. The primary objective of this research is to investigate the fundamental limits of LoRa-

based localization systems through a detailed analysis and derivation of the Cramér-Rao bound (CRB) metric for both direct position estimation and TDOA-based approaches. Additionally, we offer a performance comparison with the MLE method when employing the direct estimation approach. Therefore, the main contributions of this paper can be summarized as follows.

- We derive the MLE for position estimation using LoRa signals as direct observations, following the integrated sensing and communication (ISAC) philosophy in which communication waveforms are repurposed for sensing;
- We establish the fundamental localization limits, expressed in terms of CRLB, for both the direct and TDOA approaches. This analysis aims to establish theoretical performance benchmarks for each scenario and setting by providing closed-form expressions;
- Through extensive simulations, we investigate the localization capabilities of LoRa signals by varying key parameters, such as the SF. Our results offer valuable insights into the feasibility of practical localization using LoRa across different parameter settings.

The rest of the paper is organized as follows: Section II presents the system model and the LoRa signal used for analysis, whereas the MLE for localization problem has been addressed in Section III. Then, the bound derivations for the direct approach and TDOA and their technical concerns have been studied in Section IV. Numerical results considering the different parameters existing in LoRa are presented in Section V. At the final stage, section VI concludes the technical output of this research activity.

Notation: Throughout the paper, we use the following notation. Lowercase bold variables, e.g., $\mathbf{x}$, denote vectors. Boldface capital letters denote matrices, e.g., $\mathbf{X}$. The transpose operator is indicated by $(\cdot)^T$, the Hermitian operator is $(\cdot)^H$ and with $\odot$ being the Hadamard product. The $\mathcal{L}_2$-norm of a vector $\mathbf{r}$ is represented as $\|\mathbf{r}\|$, $\|\cdot\|_2$ represents the Euclidean norm, and j is the imaginary unit.

II. SYSTEM AND SIGNAL MODEL

A. SYSTEM MODEL AND GEOMETRY

We consider a network of N_g LoRa gateways working as receiving reference nodes to infer the location of a user equipped with a LoRa device broadcasting a signal in the surrounding environment.[1] All the N_g gateways are assumed to collaborate and share measurements with a central unit (e.g., a specific gateway or a localization engine) that processes the received signals and infers the user's position. We denote with $\mathbf{p} = [x,\ y]$ the position of the user (Tx) to be located, whereas $\mathbf{p}_g = [x_g,\ y_g]$ are the spatial coordinates of the gth gateway, with $g = 1, 2, \ldots, N_g$. Thus, the distance d_g between the transmitter and the gth gateway can be expressed as $d_g = \|\mathbf{p} - \mathbf{p}_g\|_2$.

[1] In this paper, we assume that each LoRa device is equipped with an omni-directional antenna with 0 dBi gain.

B. TRANSMITTED SIGNAL MODEL

The LoRa modulation is based on a set of linear upchirps, that is, short-duration sinusoids whose frequency $f(t)$ increases linearly, spanning a bandwidth B over a time interval T_s. Specifically, LoRa employs M uniquely shaped chirps, each representing a distinct symbol $a \in \{0, 1, \ldots, M-1\}$ of the M-ary modulation alphabet. Denoting the carrier frequency as f_c and considering the reference chirp interval $[0, T_s)$, the transmitted chirp corresponding to a generic symbol a is given by [10]

$$\bar{s}(t) = \Re\{s(t)\, e^{j2\pi f_c t}\}, \tag{1}$$

where $s(t)$ denotes the complex envelope of $\bar{s}(t)$ and it is expressed as

$$s(t) = \sqrt{P_s} \exp\left\{ j2\pi Bt \left[\frac{a}{M} - \frac{1}{2} + \frac{Bt}{2M} - u\left(t - \frac{M-a}{B}\right) \right] + j\xi \right\}, \quad 0 \le t < T_s \tag{2}$$

with P_s being the transmitted power, $u(\cdot)$ the step function, and ξ represents the initial phase of the carrier, assumed to be unknown at the receiver. Finally, the chirp duration is assumed to satisfy $T_s = M/B$ [10] as dictated by LoRa specifications.

According to (2), for each modulation symbol a, the instantaneous frequency deviation $\Delta f(t) = f(t) - f_c$ of $\bar{s}(t)$ starts at $-\frac{B}{2} + a\frac{B}{M}$ and increases linearly to $\frac{B}{2}$ with slope $\frac{B}{T_s}$. Upon reaching the maximum offset, $\Delta f(t)$ wraps around to $-\frac{B}{2}$ and continues its linear increase until the chirp duration T_s expires.

Notably, the specific modulation symbol a to be transmitted in a given chirp interval is encoded in the starting frequency of the chirp's frequency deviation, given by $-\frac{B}{2} + a\frac{B}{M}$. A noteworthy example is the chirp corresponding to the modulation symbol $a = 0$, which is a pure upchirp whose frequency deviation starts at $-\frac{B}{2}$ and reaches $\frac{B}{2}$ after T_s. Remarkably, this is the only LoRa chirp that does not exhibit any frequency wrapping.

For what follows, it is important to recall that before transmitting data according to the signal format expressed by (2), a LoRa device first transmits a preamble, which is used for frame, frequency, and time synchronization. This preamble consists of $n_{up} = 8$ pure upchirps, identical to those representing the symbol $a = 0$. Following this sequence, the device transmits n_{dw} downchirps, whose frequency deviation decreases linearly from $\frac{B}{2}$ to $-\frac{B}{2}$, marking the end of the preamble. Typically, n_{dw} is set to 2.25.

In the following, we will utilize one of the pure upchirps from the packet preamble as the reference signal for the LoRa-based localization investigated here.[2] This signal, denoted as $\bar{s}_0(t)$, is obtained from (1) and (2) by setting $a = 0$.

[2] Note that using the full preamble allows tightening the CRLB and improving localization accuracy, but it increases latency. Conversely, extending the analysis to data chirps is challenging due to the dependence of their initial frequencies on unknown symbol values.

The corresponding complex envelope, denoted as $s_0(t)$, can be immediately derived from (2) as follows

$$s_0(t) = \sqrt{P_s} \cdot \exp\left\{ j2\pi Bt\left[-\frac{1}{2} + \frac{Bt}{2M}\right] + j\xi \right\}, \ 0 \le t < T_s, \tag{3}$$

C. RECEIVED SIGNAL MODEL

Given the transmitted pure upchirp $\bar{s}_0(t)$, the RF signal received by the gth gateway can be written as

$$\bar{r}_g(t) = \rho_g\, \bar{s}_0(t - \tau_g) + \bar{w}_g(t) = \bar{y}_{g0}(t) + \bar{w}_g(t) \tag{4}$$

with $g = 1, \ldots, N_g$, where $\bar{y}_{g0}(t) = \rho_g\, \bar{s}_0(t - \tau_g)$ is the useful contribution in the received signal, $\bar{w}_g(t)$ is the additive white Gaussian noise (AWGN) modeled as a Gaussian random process with zero mean and variance σ^2, $\tau_g = d_g/c$ represents the propagation delay between the transmitter and the gth gateway, where d_g denotes the traveled distance and c is the speed of light, ρ_g is the channel gain,[3] modeled as

$$\rho_g = \sqrt{\frac{\kappa}{f_c^2\, d_g^{\beta}}}, \tag{5}$$

where $\kappa = c^2(4\pi)^{-2}$, and β accounts for the propagation exponent.[4,5]

Still focusing on the reference chirp interval $[0, T_s)$, the complex baseband signal observed at the gateway after down-conversion can be expressed as follows

$$\begin{aligned} r_g(t) &= \rho_g\, s_0(t - \tau_g) + w_g(t) \\ &= \rho_g \sqrt{P_s} \exp\left\{ j\,2\pi \left[B(t - \tau_g)\left(-\frac{1}{2} + \frac{B}{2M}(t - \tau_g)\right)\right] \right. \\ &\qquad \left. - j\,2\pi f_c \tau_g + j\xi \right\} + w_g(t) \\ &= y_{g0}(t) + w_g(t), \end{aligned} \tag{6}$$

where $y_{g0}(t) = \rho_g\, s_0(t - \tau_g)$, and $w_g(t)$ represents the baseband noise modeled as a circularly symmetric complex Gaussian random process with variance σ^2. Note also that (6) includes the additional phase term introduced by the propagation at the carrier's frequency.[6]

By sampling the received signal with a sampling interval of $T = 1/B$, the discrete-time version of (6) results in

$$\begin{aligned} r_g(kT) \triangleq r_{g,k} &= y_{g,k} + w_{g,k} = \rho_g \cdot s_{g,k} + w_{g,k} \\ &= \rho_g \sqrt{P_s} \exp \\ &\quad \times \left\{ j\,2\pi \left[B(kT - \tau_g)\left(-\frac{1}{2} + \frac{B}{2M}(kT - \tau_g)\right)\right] \right. \\ &\qquad \left. - j2\pi f_c \tau_g + j\xi \right\} + w_{g,k}, \end{aligned} \tag{7}$$

with $s_{g,k} = s_0(kT)$, $w_{g,k} = w_g(kT)$, $k \in \{0, 1, \ldots, M-1\}$, M being the number of samples in chirp interval T_s, which corresponds also to the number of modulation levels [10], [11]. Note that, by considering $BT = 1$ [10], we can finally write the useful received component $y_{g,k}$ as

$$\begin{aligned} y_{g,k} = \rho_g \sqrt{P_s} \exp &\left\{ j2\pi \left[\frac{(k - B\tau_g)^2 - M(k - B\tau_g)}{2M} \right] \right. \\ &\left. - j\,2\,\pi\, f_c\, \tau_g + j\xi \right\}. \end{aligned} \tag{8}$$

Given the signal in (7) and (8), in the following, we first derive the MLE for both the direct and TDOA approach and, successively, we will provide the expressions for the related CRLB.

III. LIKELIHOOD FUNCTION AND MLE

This section defines the MLE problem for inferring the user's position from the received signal. More specifically, the MLE aims to estimate the position $\mathbf{p} = [x, y] \in \mathbb{R}^2$ and the initial phase of the carrier ξ, based on the signal samples received at each gateway. These parameters to be estimated can be written in a vector form as $\boldsymbol{\theta} = [\mathbf{p}, \xi]$ The measurement vector is $\mathbf{r} = \left[\mathbf{r}_1, \ldots, \mathbf{r}_g, \ldots, \mathbf{r}_{N_g}\right]$, with $\mathbf{r}_g = \left[r_{g,0}, \ldots, r_{g,k}, \ldots r_{g,M-1}\right]$. The likelihood function represents the model of $\mathbf{r}$ given $\boldsymbol{\theta}$, i.e.

$$\mathbf{r} = \mathbf{y}\,(\boldsymbol{\theta}) + \mathbf{w}, \tag{9}$$

where $\mathbf{y}(\boldsymbol{\theta}) = \left[\mathbf{y}_1, \ldots, \mathbf{y}_g, \ldots, \mathbf{y}_{N_g}\right]$, with the gth element given by $\mathbf{y}_g = \left[y_{g,0}, \ldots, y_{g,k}, \ldots y_{g,M-1}\right]$, and $\mathbf{w} = \left[\mathbf{w}_1, \ldots, \mathbf{w}_g, \ldots, \mathbf{w}_{N_g}\right]$, with $\mathbf{w}_g = \left[w_{g,0}, \ldots, w_{g,k}, \ldots w_{g,M-1}\right]$.

Given the model in (9) and assuming independent measurements, we can write the likelihood function as [61, Eq. 8]

$$\begin{aligned} \ell(\mathbf{r}, \boldsymbol{\theta}) = p\,(\mathbf{r}|\boldsymbol{\theta}) &= p\left(\mathbf{r}_1, \mathbf{r}_2, \ldots, \mathbf{r}_{N_g}|\boldsymbol{\theta}\right) = \prod_{g=1}^{N_g} p\left(\mathbf{r}_g|\boldsymbol{\theta}\right) \\ &= \prod_{g=1}^{N_g} p\left(r_{g,0}, \ldots, r_{g,M-1}|\boldsymbol{\theta}\right) = \prod_{g=1}^{N_g}\prod_{k=0}^{M-1} p\left(r_{g,k}|\boldsymbol{\theta}\right), \end{aligned} \tag{10}$$

where $r_{g,k} = \Re\left\{r_{g,k}\right\} + j\Im\left\{r_{g,k}\right\}$ is a complex Gaussian random variable, i.e., $r_{g,k} \sim \mathcal{CN}(y_{g,k}, \sigma^2)$ and its real and imaginary parts are independent real Gaussian variables given by $\Re\left\{r_{g,k}\right\} \sim \mathcal{N}(\Re\left\{y_{g,k}\right\}, \sigma^2/2)$ and $\Im\left\{r_{g,k}\right\} \sim \mathcal{N}(\Im\left\{y_{g,k}\right\}, \sigma^2/2)$. Hence we can write

$$\begin{aligned} \ell(\mathbf{r}, \boldsymbol{\theta}) &= \prod_{g=1}^{N_g}\prod_{k=0}^{M-1} p\left(r_{g,k}|\boldsymbol{\theta}\right) \\ &= \prod_{g=1}^{N_g}\prod_{k=0}^{M-1} p\left(\Re\left\{y_{g,k}\right\}|\boldsymbol{\theta}\right) p\left(\Im\left\{y_{g,k}\right\}|\boldsymbol{\theta}\right) \\ &= \prod_{g=1}^{N_g}\prod_{k=0}^{M-1} \frac{1}{\pi\,\sigma^2} \exp\left(-\frac{|r_{g,k} - y_{g,k}(\boldsymbol{\theta})|^2}{\sigma^2}\right), \end{aligned} \tag{11}$$

[3] Notably, ρ_g depends on $\mathbf{p}$ (i.e., $\rho_g(\mathbf{p})$). For the rest of the paper, we will write it as ρ_g for the sake of conciseness.

[4] Different path-loss models for LoRa are discussed in [60].

[5] Our CRLB analysis is conducted under an idealized LOS channel to ensure tractability and clarity. In multipath environments, the bounds may differ, typically becoming looser. Nevertheless, in future wireless systems, multipath may also be harnessed to enhance localization performance, as discussed in [26].

[6] We assume that this phase information can be coherently retrieved to augment the existing phase data available at the LoRa transmitter.

so that the log-likelihood can be written as

$$\begin{aligned} L(\mathbf{r},\boldsymbol{\theta}) &= \ln \ell(\mathbf{r},\boldsymbol{\theta}) \\ &= \ln \frac{1}{\pi\sigma^2} - \frac{1}{\sigma^2}\sum_{g=1}^{N_g}\sum_{k=0}^{M-1}\left|r_{g,k} - \rho_g\, s_{g,k}(\boldsymbol{\theta})\right|^2 \\ &\equiv -\sum_{g=1}^{N_g}\sum_{k=0}^{M-1}\left|r_{g,k} - \rho_g\, s_{g,k}(\boldsymbol{\theta})\right|^2. \end{aligned} \tag{12}$$

Consequently, the MLE, namely, $\hat{\boldsymbol{\theta}} = [\hat{\mathbf{p}}, \hat{\xi}]$, can be formulated as

$$\hat{\boldsymbol{\theta}} = \arg\min_{\boldsymbol{\theta}} \sum_{g=1}^{N_g}\sum_{k=0}^{M-1}\left|r_{g,k} - \rho_g\, s_{g,k}(\boldsymbol{\theta})\right|^2, \tag{13}$$

which finally gives

$$\hat{\boldsymbol{\theta}} = \arg\min_{\boldsymbol{\theta}} \sum_{g=1}^{N_g}\left\{E_{y,g}(\mathbf{p}) - 2\,\Re\left\{\mathbf{r}_g\,\mathbf{y}_g^{\mathrm{H}}(\boldsymbol{\theta})\right\}\right\}, \tag{14}$$

where $E_{y,g}(\mathbf{p}) = \|\mathbf{y}_g(\boldsymbol{\theta})\|_2^2$.

The the MLE can be solved by using (i) an exhaustive grid search, (ii) a coarse grid search followed by iterative refinement using methods such as Gauss–Newton or gradient descent, or (iii) multi-start local optimization to reduce the risk of local minima.

In the following, we derive the CRLB for both the direct and the TDOA approaches.

IV. LOCALIZATION PERFORMANCE LIMITS

The performance of any unbiased estimator $\hat{\boldsymbol{\theta}}$ can be bounded by the CRLB defined as [62]

$$\begin{aligned} \mathrm{MSE}\left(\hat{\boldsymbol{\theta}}\right) &= \mathbb{E}\left\{\left[\hat{\boldsymbol{\theta}} - \boldsymbol{\theta}\right]\left[\hat{\boldsymbol{\theta}} - \boldsymbol{\theta}\right]^H\right\} \succcurlyeq \mathbf{J}^{-1}(\boldsymbol{\theta}) \\ &= \mathsf{CRB}(\boldsymbol{\theta}), \end{aligned} \tag{15}$$

where $\succcurlyeq$ indicates that $\mathrm{MSE}\left(\hat{\boldsymbol{\theta}}\right) - \mathsf{CRB}(\boldsymbol{\theta})$ is semi-positive definite. $\mathbf{J}$ is the FIM defined as

$$\begin{aligned} [\mathbf{J}(\boldsymbol{\theta})]_{i,j} &\triangleq \mathbb{E}\left[\frac{\partial L(\mathbf{r},\boldsymbol{\theta})}{\partial[\boldsymbol{\theta}]_i}\cdot\frac{\partial L(\mathbf{r},\boldsymbol{\theta})}{\partial[\boldsymbol{\theta}]_j}\right] \\ &= -\mathbb{E}\left[\frac{\partial^2 L(\mathbf{r},\boldsymbol{\theta})}{\partial[\boldsymbol{\theta}]_i\,\partial[\boldsymbol{\theta}]_j}\right], \end{aligned} \tag{16}$$

where the operators $[\cdot]_a$ and $[\cdot]_{a,b}$ respectively pick the a-th or the (a-row, b-column) entry of its argument, and $L(\mathbf{r},\boldsymbol{\theta})$ is the log-likelihood function of $\boldsymbol{\theta}$ given the measurements in $\mathbf{r}$.

In the following, we first examine the direct approach, which accounts for the LoRa signal model in (8) to directly estimate $\boldsymbol{\theta}$. We then focus on the TDOA-based approach, which, due to the use of TDOA measurements, allows for a simpler derivation. Then, their attainable performance are compared and discussed in Sec. V.

A. DIRECT APPROACH

We now consider a direct approach, which estimates directly $\boldsymbol{\theta}$ without relying on intermediate parameters. Thus, in this case, it holds

$$\mathbf{J}(\boldsymbol{\theta}) = \sum_{g=1}^{N_g}\mathbf{J}_g(\boldsymbol{\theta}), \tag{17}$$

where the FIM at each gateway, namely $\mathbf{J}_g(\boldsymbol{\theta})$, is defined as

$$\mathbf{J}_g(\boldsymbol{\theta}) \triangleq \mathbb{E}_{\mathbf{r}_g}\left[\nabla_{\boldsymbol{\theta}} L\left(\mathbf{r}_g,\boldsymbol{\theta}\right)\nabla_{\boldsymbol{\theta}}^H L\left(\mathbf{r}_g,\boldsymbol{\theta}\right)\right], \tag{18}$$

with $\nabla_{\boldsymbol{\theta}} = \left[\frac{\partial}{\partial x}, \frac{\partial}{\partial y}, \frac{\partial}{\partial \xi}\right]^T$ being the gradient operator.

In the following, we will denote $\mathbf{J}_g(\boldsymbol{\theta}) = \mathbf{J}_g$, $\mathbf{y}_g(\boldsymbol{\theta}) = \mathbf{y}_g$ for the sake of conciseness. The generic elements of the g-th FIM related to the gth gateway can be expressed as

$$\left[\mathbf{J}_g\right]_{i,j} = \frac{2}{\sigma^2}\,\Re\left\{\frac{\partial \mathbf{y}_g}{\partial[\boldsymbol{\theta}]_i}\cdot\frac{\partial \mathbf{y}_g^H}{\partial[\boldsymbol{\theta}]_j}\right\}, \tag{19}$$

$$= \frac{2}{\sigma^2}\sum_{k=0}^{M-1}\Re\left\{\frac{\partial y_{g,k}}{\partial[\boldsymbol{\theta}]_i}\cdot\frac{\partial y_{g,k}^{\star}}{\partial[\boldsymbol{\theta}]_j}\right\}. \tag{20}$$

By considering the position coordinates, and by following the steps reported in Appendix A, we can write

$$\frac{\partial y_{g,k}}{\partial[\boldsymbol{\theta}]_1} = \frac{\partial y_{g,k}}{\partial x} = y_{g,k}\frac{(x-x_g)}{d_g^2}\left[-\frac{\beta}{2} + j d_g A_{g,k}^{(1)}\right], \tag{21}$$

$$\frac{\partial y_{g,k}}{\partial[\boldsymbol{\theta}]_2} = \frac{\partial y_{g,k}}{\partial y} = y_{g,k}\frac{(y-y_g)}{d_g^2}\left[-\frac{\beta}{2} + j d_g A_{g,k}^{(1)}\right], \tag{22}$$

with

$$A_{g,k}^{(1)} = \frac{B\pi}{Mc}\left[M + 2B\tau_g - 2\,k - 2M\frac{f_c}{B}\right], \tag{23}$$

that is the phase rate with respect to the delay. This shows that the term $j\,d_g\,A_{g,k}^{(1)}$ appearing in (21) and (22) represents the phase sensitivity to delay and it is directly tied to the instantaneous frequency of the LoRa chirp at time index k. Finally, the derivative related to the initial phase offset is given by

$$\frac{\partial y_{g,k}}{\partial[\boldsymbol{\theta}]_3} = \frac{\partial\, y_{g,k}}{\partial \xi} = j y_{g,k}. \tag{24}$$

Then, according to the expressions for $\left[\mathbf{J}_g\right]_{i,j}$ provided in Appendix A, and by letting α_g being the angle between the g-th gateway and the transmitter, $\gamma_g = \frac{P_s\rho_g^2}{\sigma^2}$, the FIM elements in the diagonal can be written as

$$[\mathbf{J}]_{1,1} = 2\sum_{g=1}^{N_g}\frac{\gamma_g\,\Gamma_g}{d_g^2}\left(\frac{x-x_g}{d_g}\right)^2 = 2\sum_{g=1}^{N_g}\frac{\gamma_g\,\Gamma_g}{d_g^2}c_{\alpha_g}^2, \tag{25}$$

$$[\mathbf{J}]_{2,2} = 2\sum_{g=1}^{N_g}\frac{\gamma_g\,\Gamma_g}{d_g^2}\left(\frac{y-y_g}{d_g}\right)^2 = 2\sum_{g=1}^{N_g}\frac{\gamma_g\,\Gamma_g}{d_g^2}s_{\alpha_g}^2, \tag{26}$$

$$[\mathbf{J}]_{3,3} = 2M\sum_{g=1}^{N_g}\gamma_g, \tag{27}$$

where $c_{\alpha_g} \triangleq \cos(\alpha_g) = (x - x_g)/d_g$, $s_{\alpha_g} \triangleq \sin(\alpha_g) = (y - y_g)/d_g$, and

$$\begin{aligned}\Gamma_g &= \sum_{k=0}^{M-1} \left| -\frac{\beta}{2} + j\, d_g\, A_{g,k}^{(1)} \right|^2 \\ &= \frac{M\beta^2}{4} + \frac{\left(\tau_g\, B\, \pi\right)^2}{M} \\ &\quad \times \left[\frac{M^2}{3} + 4\frac{M^2 f_c^2}{B^2} - 4\, M \frac{f_c}{B} - 8\, M\, \tau_g f_c + 4\, B^2\, \tau_g^2 \right. \\ &\quad \left. \times + 4\, B\, \tau_g + \frac{2}{3} \right]. \end{aligned} \tag{28}$$

Then, by defining

$$\Omega_g = \sum_{k=0}^{M-1} A_{g,k}^{(1)} = \left(\frac{B\,\pi}{c}\right)\left(2B\tau_g + 1 - 2M\frac{f_c}{B}\right), \tag{29}$$

the FIM cross-terms are given by

$$[\mathbf{J}]_{1,2} = [\mathbf{J}]_{2,1} = 2\sum_{g=1}^{N_g} \frac{\gamma_g\, \Gamma_g}{d_g^2}\, c_{\alpha_g}\, s_{\alpha_g}, \tag{30}$$

$$[\mathbf{J}]_{3,1} = [\mathbf{J}]_{1,3} = 2\sum_{g=1}^{N_g} \gamma_g \Omega_g c_{\alpha_g}, \tag{31}$$

$$[\mathbf{J}]_{3,2} = [\mathbf{J}]_{2,3} = 2\sum_{g=1}^{N_g} \gamma_g \Omega_g s_{\alpha_g}. \tag{32}$$

Consequently, the FIM can be written as

$$\mathbf{J} = 2\sum_{g=1}^{N_g} \gamma_g\, \mathbf{A}_g \odot \mathbf{G}_g, \tag{33}$$

where $\mathbf{A}_g$ and $\mathbf{G}_g$ are matrices that depend on LoRa signaling properties and geometrical characteristics, respectively, and they are given by

$$\mathbf{A}_g = \left[\begin{array}{c|c} \frac{\Gamma_g}{d_g^2}\, \mathbf{1}_{2\times 2} & \Omega_g\, \mathbf{1}_{2\times 1} \\ \hline \Omega_g\, \mathbf{1}_{1\times 2} & 1 \end{array}\right], \tag{34}$$

$$\mathbf{G}_g = \left[\begin{array}{cc|c} c_{\alpha_g}^2 & c_{\alpha_g} s_{\alpha_g} & c_{\alpha_g} \\ c_{\alpha_g} s_{\alpha_g} & s_{\alpha_g}^2 & s_{\alpha_g} \\ \hline c_{\alpha_g} & s_{\alpha_g} & 1 \end{array}\right], \tag{35}$$

with $\mathbf{1}_{N\times M}$ being a matrix of all ones with size $N \times M$.

Finally, we define the position error bound (PEB) and the synchronization error bound (SEB) as

$$\begin{aligned} \mathsf{PEB} &= \sqrt{\mathrm{tr}\{\mathbf{J}^{-1}\}_{1:2,1:2}}, \\ \mathsf{SEB} &= \sqrt{\{\mathbf{J}^{-1}\}_{3,3}}. \end{aligned} \tag{36}$$

By indicating with $\gamma_{\mathrm{tot}} \triangleq \sum_{g=1}^{N_g} \gamma_g$, $\eta_g \triangleq \frac{\gamma_g \Gamma_g}{d_g^2}$, and with

$$\begin{aligned}\det(\mathbf{J}) &= [\mathbf{J}]_{1,1}\left([\mathbf{J}]_{2,2}[\mathbf{J}]_{3,3} - [\mathbf{J}]_{2,3}^2\right) \\ &\quad - [\mathbf{J}]_{1,2}\left([\mathbf{J}]_{2,1}[\mathbf{J}]_{3,3} - [\mathbf{J}]_{2,3}[\mathbf{J}]_{3,1}\right) \\ &\quad + [\mathbf{J}]_{1,3}\left([\mathbf{J}]_{2,1}[\mathbf{J}]_{3,2} - [\mathbf{J}]_{2,2}[\mathbf{J}]_{3,1}\right), \end{aligned} \tag{37}$$

we can write

$$\mathsf{PEB} = \sqrt{\frac{4M\gamma_{\mathrm{tot}}\sum_{g=1}^{N_g}\eta_g - 4\left(\sum_{g=1}^{N_g}\gamma_g\Omega_g s_{\alpha_g}\right)^2 - 4\left(\sum_{g=1}^{N_g}\gamma_g\Omega_g c_{\alpha_g}\right)^2}{\det(\mathbf{J})}}, \tag{38}$$

$$\mathsf{SEB} = \sqrt{\frac{4\sum_{g=1}^{N_g}\eta_g c_{\alpha_g}^2 \sum_{\ell=1}^{N_g}\eta_\ell s_{\alpha_\ell}^2 - \left(2\sum_{g=1}^{N_g}\eta_g c_{\alpha_g} s_{\alpha_g}\right)^2}{\det(\mathbf{J})}}. \tag{39}$$

Note that, due to $\det(\mathbf{J})$, the two expressions above do not allow to achieve an easy interpretation of the PEB and SEB.[7]

Then, in order to find more compact and interpretable expressions, we observe that, in the perfect synchronous case, i.e., by neglecting the synchronization error in $\boldsymbol{\theta}$, the CRB reduces to a 2×2 matrix such that the expression of $\det(\mathbf{J})$ can be simplified as

$$\begin{aligned}\det(\mathbf{J}) &= [\mathbf{J}]_{1,1}[\mathbf{J}]_{2,2} - [\mathbf{J}]_{1,2}^2 \\ &= 4\left(\sum_{g=1}^{N_g}\eta_g\, c_{\alpha_g}^2 \sum_{\ell=1}^{N_g}\eta_\ell\, s_{\alpha_\ell}^2 - \left(\sum_{g=1}^{N_g}\eta_g\, c_{\alpha_g} s_{\alpha_g}\right)^2\right) \end{aligned} \tag{40}$$

so that the PEB, in the absence of ξ in $\boldsymbol{\theta}$ (i.e., in the synchronous case), can be expressed as

$$\begin{aligned}\mathsf{PEB}_{\mathrm{synch}} &= \sqrt{\frac{[\mathbf{J}]_{1,1} + [\mathbf{J}]_{2,2}}{\det(\mathbf{J})}} \\ &= \sqrt{\frac{\sum_{g=1}^{N_g}\eta_g}{2\left(\sum_{g=1}^{N_g}\eta_g c_{\alpha_g}^2 \sum_{\ell=1}^{N_g}\eta_\ell s_{\alpha_\ell}^2 - \left(\sum_{g=1}^{N_g}\eta_g c_{\alpha_g} s_{\alpha_g}\right)^2\right)}}. \end{aligned} \tag{41}$$

As evidenced in (41), the $\mathsf{PEB}_{\mathrm{synch}}$ is impacted by the SNR and LoRa parameters in η_g, as well as by the geometry highlighted through c_{α_g} and s_{α_g}.

B. REMARKS

1) REMARK 1

We have seen, for the direct approach, how to derive the PEB in the presence and absence of synchronization offset among the parameters to be estimated in $\boldsymbol{\theta}$. Here, we observe also that by denoting the equivalent FIM elements as

$$\begin{aligned}\mathbf{J}_{\mathbf{pp}} &= \begin{bmatrix} [\mathbf{J}]_{11} & [\mathbf{J}]_{12} \\ [\mathbf{J}]_{21} & [\mathbf{J}]_{22} \end{bmatrix}, \\ \mathbf{J}_{\xi\xi} &= [\mathbf{J}]_{33}, \\ \mathbf{J}_{\mathbf{p}\xi} &= [[\mathbf{J}]_{13},\, [\mathbf{J}]_{23}], \end{aligned} \tag{42}$$

[7] It is important to remark that $\det(\mathbf{J})$ also reflects the geometric configuration of the gateways. In particular, unfavorable placements, such as collinear or clustered arrangements, lead to smaller values of $\det(\mathbf{J})$ and, consequently, larger values of PEB.

the PEB can be alternatively expressed, using the Schur complement, as

$$\mathsf{PEB} = \sqrt{\left(\mathbf{J}_{\mathbf{pp}} - \mathbf{J}_{\mathbf{p}\xi}\mathbf{J}_{\xi\xi}^{-1}\mathbf{J}_{\mathbf{p}\xi}^{H}\right)^{-1}}, \tag{43}$$

where the argument of the root-square corresponds to the first block of the CRB matrix when the synchronization offset is included as a nuisance parameter. Instead, by neglecting the synchronization offset in $\boldsymbol{\theta}$, we have for the synchronous scenario

$$\mathsf{PEB}_{\text{synch}} = \sqrt{\left(\mathbf{J}_{\mathbf{pp}}\right)^{-1}}. \tag{44}$$

According to these expressions, the impact of position and synchronization parameters on each other can be numerically evaluated by analyzing the cross-correlation matrix $\mathbf{J}_{\mathbf{p}\xi}$, as will be done in Sec. V-B.

2) REMARK 2

By ignoring the off-diagonal elements of the FIM, i.e. the correlation among various elements in the FIM matrix, the PEB in (38) and the SEB in (39) can be upper bounded as

$$\mathsf{PEB} \leq \sqrt{[\mathbf{J}]_{11}^{-1} + [\mathbf{J}]_{22}^{-1}} = \sqrt{\frac{\sum_{g=1}^{N_g}\eta_g}{2\sum_{g=1}^{N_g}\eta_g c_{\alpha_g}^2 \cdot \sum_{\ell=1}^{N_g}\eta_\ell s_{\alpha_\ell}^2}}, \tag{45}$$

$$\mathsf{SEB} \leq \sqrt{[\mathbf{J}]_{33}^{-1}} = \sqrt{\frac{1}{2\gamma_{\text{tot}}}}. \tag{46}$$

As also verified numerically, the off-diagonal elements of the FIM are often much smaller than the elements along the diagonal, suggesting that approximated expressions of the PEB and SEB can be retrieved by accounting for the upper bounds in the right-hand side terms of (45) and (46), respectively.

C. TDOA-BASED APPROACH

In this section, we derive the CRLB by considering a two-step approach [63]. First, we will consider the CRLB on user position starting from TDOA measurements. Then, to model the statistics of TDOA measurements, we derive the CRLB on TOA starting from the received signals. The advantage of using the TDOA-based approach is that it effectively resolves the synchronization offset ξ, providing a valuable solution for comparing the performance achieved with the direct approach.

In the TDOA-based approach, we identify a gateway as the reference one, and the others compute the difference of the estimated TOA with respect to it. This operation allows to eliminate the impact of the synchronization phase offset, so that, $\boldsymbol{\theta} = \mathbf{p}$. In the sequel, without loss of generality, we will consider the gateway indexed with 1 as the reference one.[8] In this case, the measurement vector containing the TDOAs is

$$\boldsymbol{\eta} = [\widehat{\Delta\tau}_2, .., \widehat{\Delta\tau}_g, .., \widehat{\Delta\tau}_{N_g}], \tag{47}$$

where the TDOA at a generic gateway is given by

$$\widehat{\Delta\tau}_g = \Delta\tau_g(\mathbf{p}) + n_g \sim \mathcal{N}\left(\Delta\tau_g(\mathbf{p}), \sigma_{\Delta\tau_g}^2\right), \tag{48}$$

with

$$\Delta\tau_g(\mathbf{p}) = \tau_g(\mathbf{p}) - \tau_1(\mathbf{p}) = \frac{\|\mathbf{p}-\mathbf{p}_g\|_2}{c} - \frac{\|\mathbf{p}-\mathbf{p}_1\|_2}{c}. \tag{49}$$

To model the noise variance of TDOA measurements, the estimation error is assumed Gaussian with variance $\sigma_{\Delta\tau_g}^2 = 2\sigma_{\tau_g}^2$, where $\sigma_{\tau_g}^2$ is the variance for estimating τ_g and that will be characterized in the next section through the computation of the CRLB related to the TOA.

Then, according to [64], the FIM on the user position given TDOA measurements can be written as

$$\mathbf{J}(\mathbf{p}) \triangleq \mathbb{E}_{\boldsymbol{\eta}}\left[\nabla_{\mathbf{p}} L(\boldsymbol{\eta}, \mathbf{p}) \nabla_{\mathbf{p}}^{T} L(\boldsymbol{\eta}, \mathbf{p})\right], \tag{50}$$

with $\boldsymbol{\eta}$ defined in (47) and

$$\nabla_{\mathbf{p}} L(\boldsymbol{\eta}, \mathbf{p}) = -\sum_{g=2}^{N_g} \frac{1}{\sigma_{\Delta\tau_g}^2}(\widehat{\Delta\tau}_g - \Delta\tau_g)\nabla_{\mathbf{p}}\Delta\tau_g. \tag{51}$$

Note that we neglected the information about the position encapsulated in the noise variance, as extracting such information is typically challenging. Hence, it is straightforward to obtain

$$\mathbf{J}(\mathbf{p}) = \sum_{g=2}^{N_g}\mathbf{J}_g(\mathbf{p}) = \sum_{g=2}^{N_g}\frac{1}{\sigma_{\Delta\tau_g}^2}\nabla_{\mathbf{p}}^{T}\Delta\tau_g\,\nabla_{\mathbf{p}}\Delta\tau_g, \tag{52}$$

where

$$\begin{aligned}\frac{\partial\Delta\tau_g}{\partial x} &= \frac{1}{c}\left(\frac{x-x_g}{d_g} - \frac{x-x_1}{d_1}\right) = \frac{1}{c}\left(c_{\alpha_g} - c_{\alpha_1}\right),\\ \frac{\partial\Delta\tau_g}{\partial y} &= \frac{1}{c}\left(\frac{y-y_g}{d_g} - \frac{y-y_1}{d_1}\right) = \frac{1}{c}\left(s_{\alpha_g} - s_{\alpha_1}\right).\end{aligned} \tag{53}$$

and $d_1 \triangleq \|\mathbf{p}-\mathbf{p}_1\|_2$. Let define

$$v_g^{(x)} = \left(\frac{c_{\alpha_g} - c_{\alpha_1}}{c}\right)^2, \tag{54}$$

$$v_g^{(y)} = \left(\frac{s_{\alpha_g} - s_{\alpha_1}}{c}\right)^2, \tag{55}$$

$$v_g^{(x,y)} = \frac{\left(c_{\alpha_g} - c_{\alpha_1}\right)\left(s_{\alpha_g} - s_{\alpha_1}\right)}{c^2}. \tag{56}$$

According to these definitions, the FIM elements can be written as

$$\begin{aligned}[\mathbf{J}]_{11} &= \sum_{g=2}^{N_g}\frac{v_g^{(x)}}{\sigma_{\Delta\tau_g}^2},\\ [\mathbf{J}]_{22} &= \sum_{g=2}^{N_g}\frac{v_g^{(y)}}{\sigma_{\Delta\tau_g}^2},\\ [\mathbf{J}]_{12} &= [\mathbf{J}]_{21} = \sum_{g=2}^{N_g}\frac{v_g^{(x,y)}}{\sigma_{\Delta\tau_g}^2}.\end{aligned} \tag{57}$$

[8] Different solutions can be envisioned to select the reference gateway, for example, based on the level of experienced SNR.

Therefore, we can find the PEB as

$$\text{PEB} = \sqrt{\frac{\sum_{g=2}^{N_g} \frac{v_g^{(x)}}{\sigma^2_{\Delta\tau_g}} + \sum_{g=2}^{N_g} \frac{v_g^{(y)}}{\sigma^2_{\Delta\tau_g}}}{\sum_{g=2}^{N_g} \frac{v_g^{(x)}}{\sigma^2_{\Delta\tau_g}} \cdot \sum_{g=2}^{N_g} \frac{v_g^{(y)}}{\sigma^2_{\Delta\tau_g}} - \left(\sum_{g=2}^{N_g} \frac{v_g^{(x,y)}}{\sigma^2_{\Delta\tau_g}}\right)^2}}. \tag{58}$$

Notably, the PEB is affected by the geometric terms $v_g^{(x)}$ and $v_g^{(y)}$, as well as by $\sigma^2_{\Delta\tau_g}$ which contains all the peculiarities related to the LoRa signaling scheme.

In the following, we will provide insights about the derivation of $\sigma^2_{\Delta\tau_g}$.

1) DEFINITION OF $\sigma^2_{\Delta\tau_G}$

In order to define $\sigma^2_{\Delta\tau_g}$, we need to find an expression for $\sigma^2_{\tau_g}$. For this purpose, we derive the fundamental limits for estimating the TOA parameter τ_g. Following the same derivations as per the direct approach, the FIM associated with the delay at the g-th gateway can be written as

$$J\left(\tau_g\right) = \sum_{k=0}^{M-1} \frac{2}{\sigma^2} \Re\left\{\frac{\partial y_{g,k}}{\partial \tau_g} \cdot \frac{\partial y^{\star}_{g,k}}{\partial \tau_g}\right\}, \tag{59}$$

and according to Appendix B, we can write

$$\frac{\partial y_{g,k}}{\partial \tau_g} = y_{g,k}\left[-\frac{\beta}{2\tau_g} + j2\pi A^{(2)}_{g,k}\right], \tag{60}$$

where

$$A^{(2)}_{g,k} = \frac{-2\,k\,B^2\,T + 2B^2\tau_g + MB - 2Mf_c}{2M}. \tag{61}$$

Thus, (59) can be written as

$$\begin{aligned} J\left(\tau_g\right) &= 2\gamma_g \sum_{k=0}^{M-1} \left\{\left[\frac{\beta^2}{4\tau_g^2} + 4\pi^2\left(A^{(2)}_{g,k}\right)^2\right]\right\} \\ &= \frac{\gamma_g\,M\,\beta^2}{2\tau_g^2} + 8\pi^2\gamma_g \sum_{k=0}^{M-1}\left(A^{(2)}_{g,k}\right)^2, \end{aligned} \tag{62}$$

so that it holds

$$\sigma^2_{\tau_g} = J^{-1}(\tau_g) = \frac{1}{\frac{\gamma_g\,M\,\beta^2}{2\tau_g^2} + 8\pi^2\gamma_g \sum_{k=0}^{M-1}\left(A^{(2)}_{g,k}\right)^2}. \tag{63}$$

Finally, we find the expression of $\sigma^2_{\Delta\tau_g}$ as

$$\sigma^2_{\Delta\tau_g} = 2\,\sigma^2_{\tau_g} = \frac{4\tau_g^2}{\gamma_g\,M\beta^2 + 16\pi^2\gamma_g\tau_g^2 \sum_{k=0}^{M-1}\left(A^{(2)}_{g,k}\right)^2}, \tag{64}$$

which is different for each gateway, in accordance with its distance to the transmitter, and that can be expressed as in (65), shown at the bottom of the page.

TABLE 1. Simulation parameters.

Symbol	Value
Signal Bandwidth B	125 kHz
Central Frequency f_c	868 MHz
Transmitted Power P_s	from -9 to 6 dBm
Power Spectral Density N_0	-204 dBW/Hz
Propagation constant κ	$c^2(4\pi)^{-2} \simeq 5.7 \cdot 10^{14}$
Propagation Exponent β	2.6, 3.6
# Gateways N_g	4, 8, 16
Environment size A_x, A_y	2000 m
Gateway coordinates $\mathbf{p}_g$	$N_g = 4$: $(0,0), (A_x,0), (0,A_y), (A_x,A_y)$ $N_g = 8$: $(0,0), (A_x,0), (0,A_y)$ $(A_x,A_y), (\frac{A_x}{2},0), (A_x,\frac{A_y}{2})$ $(\frac{A_x}{2},A_y), (0,\frac{A_y}{2})$ $N_g = 16$: $(\frac{A_x}{5},0), (\frac{2A_x}{5},0), (\frac{3A_x}{5},0)$ $(\frac{4A_x}{5},0), (\frac{A_x}{5},A_y), (\frac{2A_x}{5},A_y)$ $(\frac{3A_x}{5},A_y), (\frac{4A_x}{5},A_y), (0,\frac{A_y}{5})$ $(A_x,\frac{A_y}{5}), (0,\frac{2A_y}{5}), (A_x,\frac{2A_y}{5})$ $(0,\frac{3A_y}{5}), (A_x,\frac{3A_y}{5}), (0,\frac{4A_y}{5})$ $(A_x,\frac{4A_y}{5})$

In the following, we evaluate the attainable performance in accordance with the derived expression of the MLE and the CRLB.

V. NUMERICAL RESULTS

In this section, by assessing the previously derived expressions, we evaluate LoRa-based localization performance, considering both fundamental limits and MLE results.

A. SIMULATION SETTINGS

We considered an area of $(A_x \times A_y) = (2 \times 2)\,\text{km}^2$, with gateways positioned along its perimeter, aimed at localizing a LoRa device transmitter placed within the area.

Regarding the considered LoRa signaling parameters, we accounted for a signal bandwidth of $B = 125$ kHz, a carrier frequency of $f_c = 868$ MHz and a propagation path loss exponent of $\beta = 2.6$ or $\beta = 3.6$. Parameters such as the TX power P_s are specified on a per-test basis. The main parameters are reported in Table 1. When $N_g = 4$ gateways are considered, they are placed at the corners of the environment, whereas with $N_g = 8$, they are placed at the four corners and in $(A_x/2, 0)$, $(A_x, A_y/2)$, $(A_x/2, A_y)$, $(0, A_y/2)$. Finally, when $N_g = 16$, gateways are located in $(A_x/5, 0)$, $(2A_x/5, 0)$, $(3A_x/5, 0)$, $(4A_x/5, 0)$, $(A_x/5, A_y)$, $(2A_x/5, A_y)$, $(3A_x/5, A_y)$, $(4A_x/5, A_y)$, $(0, A_y/5)$, $(A_x, A_y/5)$, $(0, 2A_y/5)$, $(A_x, 2A_y/5)$, $(0, 3A_y/5)$, $(A_x, 3A_y/5)$, $(0, 4A_y/5)$, $(A_x, 4A_y/5)$.

$$\sigma^2_{\Delta\tau_g} = \frac{12\,M\tau_g^2}{3\,\gamma_g\,M\beta^2 + 4\pi^2\gamma_g\tau_g^2\left(12B^4\tau_g^2 + 12B^3\tau_g + B^2M^2 - 24B^2\,Mf_c\tau_g + 2B^2 - 12\,BMf_c + 12\,M^2f_c^2\right)}. \tag{65}$$

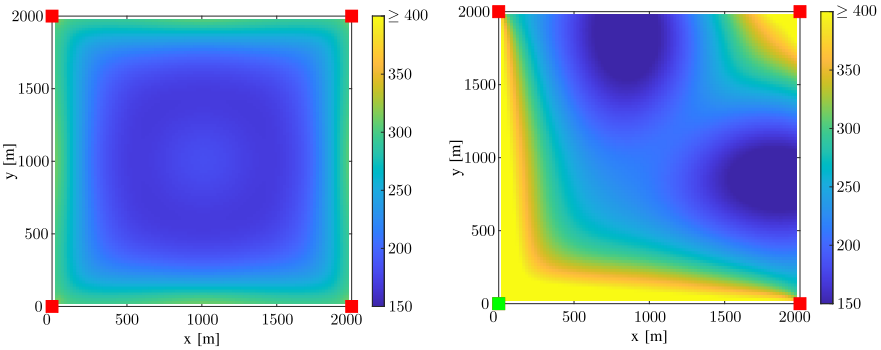

FIGURE 1. PEB maps (in meters) obtained when neglecting the carrier phase information in (8), and with $\beta = 2.6$. Left: direct approach and closed formula without synchronization offset ($\text{PEB}_{\text{synch}}$ in (41)). Right: TDOA ((57)). Red squares refer to gateways, whereas the green one refers to the reference for TDOA.

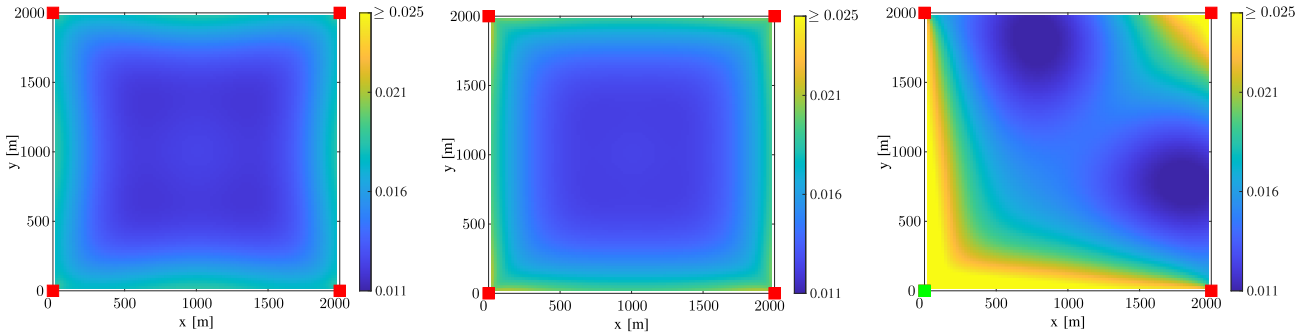

FIGURE 2. PEB maps (in meters) with carrier phase information (i.e., obtained starting from (8)) and with $\beta = 2.6$. Left: direct approach and closed formula without synchronization offset ($\text{PEB}_{\text{synch}}$ in (41)). Middle: direct approach and synchronization offset ((38)). Right: TDOA ((57)). Red squares refer to gateways, whereas the green one refers to the reference for TDOA.

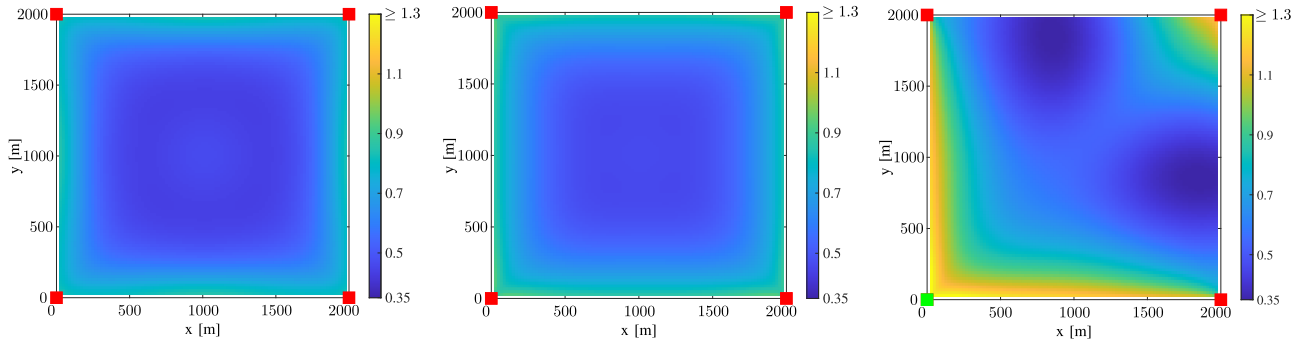

FIGURE 3. PEB maps (in meters) with carrier phase information (i.e., obtained starting from (8)) and with $\beta = 3.6$. Left: direct approach and closed formula without synchronization offset ($\text{PEB}_{\text{synch}}$ in (41)). Middle: direct approach and synchronization offset ((38)). Right: TDOA ((57)). Red squares refer to gateways, whereas the green one refers to the reference for TDOA.

B. FUNDAMENTAL LOCALIZATION LIMITS

We first present the obtained PEB results with the transmitter positioned at the center of the environment, i.e., at $(1000, 1000)$ m, and with $N_{\text{g}} = 4$. Then, PEB values were obtained across three configurations and by using the previous derivations: (1) in the synchronous case, i.e., by accounting for $\text{PEB}_{\text{synch}}$; (2) with synchronization offset; and (3) using TDOA measurements. We also evaluated the impact of the phase information related to the carrier frequency f_{c} by accounting and neglecting its contribution in (8).

1) ANALYSIS OF THE LoRa PARAMETERS IMPACT

In this context, Table 2 presents the obtained CRLB values. As expected, the availability of phase information at the carrier frequency significantly reduces the PEB values under identical conditions. Furthermore, the results indicate that the

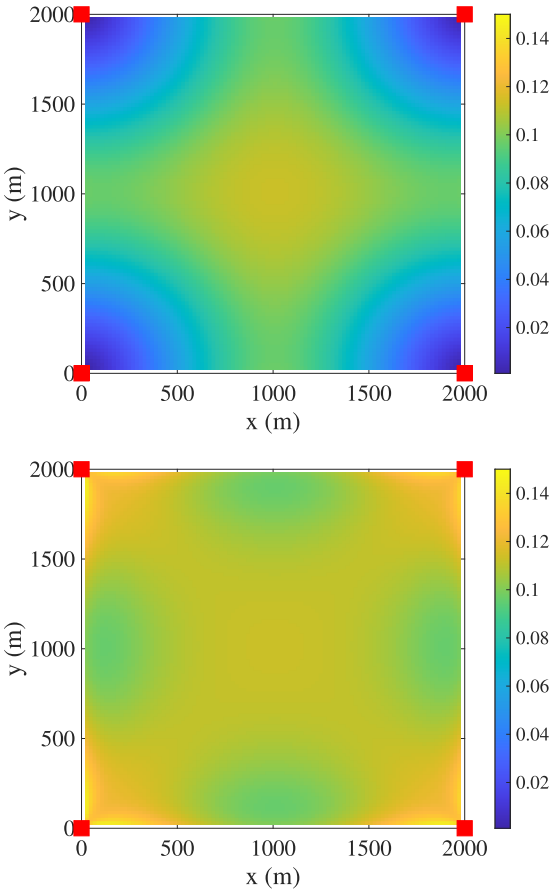

FIGURE 4. SEB in radians obtained for $\beta = 2.6$ and without (top) or with (bottom) carrier phase information.

TABLE 2. PEB under different conditions, when the transmitter is located in (1000, 1000) m. In the case with $N_g = 4$ and $\beta = 2.6$, it holds $\gamma_g \simeq 1$ dB for each gateway, whereas, for $N_g = 4$ and $\beta = 3.6$, it holds $\gamma_g \simeq -29$ dB for each gateway.

Without carrier phase information	Direct	TDOA
$N_g = 4, \beta = 2.6$, SF $= 3$	181.85 m	291.73 m
$N_g = 4, \beta = 2.6$, SF $= 7$	47.31 m	85.51 m
$N_g = 4, \beta = 2.6$, SF $= 12$	8.37 m	15.21 m
$N_g = 4, \beta = 3.6$, SF $= 12$	252.91 m	571.79 m
$N_g = 8, \beta = 3.6$, SF $= 12$	95.20 m	270.01 m
$N_g = 16, \beta = 3.6$, SF $= 12$	62.61 m	176.46 m
With carrier phase information	Direct	TDOA
$N_g = 4, \beta = 3.6$, SF $= 3$	0.47 m	0.54 m
$N_g = 4, \beta = 3.6$, SF $= 7$	0.11 m	0.13 m
$N_g = 4, \beta = 3.6$, SF $= 12$	0.02 m	0.03 m

SF has a strong impact within the considered configurations since larger SF values imply an increase in the overall received energy within the chirp interval. It is also worth noting that, while the PEB achieves sub-meter accuracy under the configurations with carrier phase information, the MLE results presented in the next section reveal that ambiguities in the search process have a substantial effect, leading to significant performance degradation. It is also important to note that employing a large number of gateways, i.e., $N_g = 16$, can significantly improve performance even without exploiting the carrier phase information and with $\beta = 3.6$.

2) PEB MAPS

We pick SF $= 3$ and $P_s = -9$ dBm,[9] and, in Fig. 1-Fig. 3, we report the achieved PEB maps evaluated in the environment with an area $A_x \times A_y$ for various locations of the LoRa device. Each PEB map is derived either by accounting for the phase information on the carrier frequency (Fig. 2 and Fig. 3), or not (Fig. 1). Results corroborated those reported in Table 2. First, as reported in Fig. 1, we observe that, when the carrier phase information is not available (i.e., when accounting for the signal in (8) without the terms with f_c and ξ), PEB performance is very poor with errors of hundreds of meters. To improve performance, either it is required to increase the number of gateways, namely, N_g or the SF value (see Table 2). On the other way round, when the phase information on the carrier frequency is included (see Fig.2 and Fig. 3 performance is very good even in challenging setups (e.g., $\beta = 3.6$). This is due to the combined use of signal strength and phase information, which, under ideal propagation conditions, enables a highly accurate estimation process both for $\beta = 2.6$ and $\beta = 3.6$.

a: ANALYSIS OF THE PHASE OFFSET ξ IMPACT

We observe that the phase offset ξ has only a limited impact on performance (see the differences in Fig. 1–Fig. 3 between the maps on the left and their counterparts in the middle).

The fact that the PEB remains nearly unchanged suggests that estimating ξ does not enhance position estimation. This behavior indicates that the cross-correlation terms $\mathbf{J}_{\mathbf{p}\xi}$ in (43) are approximately zero, meaning that the position and synchronization parameters are nearly orthogonal in the Fisher information sense. As a result, estimating ξ provides little to no improvement in positioning accuracy.

Furthermore, this effect can also be attributed to the use of multiple gateways (e.g., four) for localization. With several independent measurements, the system can effectively resolve position information even in the presence of an unknown phase offset, thereby reducing the influence of ξ on overall accuracy.

In summary, we have two situations: *(i)* the phase offset is excluded from the parameter vector and, thus, its value is assumed to be known, so that its impact on the PEB is eliminated; *(ii)* the phase offset is included in the parameter vector and, thus, it is treated as an unknown nuisance parameter. But since we always consider at least 4 gateways and only $\mathbf{p}$ and ξ need to be estimated, even in case *(ii)* the phase offset can still be determined, resulting in nearly the same outcome as in case *(i)*.

[9]Even though SF $= 3$ and $P_s = -9$ dBm are not commonly employed in LoRa systems, since $7 \leq$ SF ≤ 12, and -4 dBm $\leq P_s \leq 20$ dBm, we use these numbers here as they allow to achieve interesting performance in the considered setup.

3) SEB MAPS

Considering these aspects, Fig. 4 illustrates the SEB for $\beta = 2.6$ under two scenarios: with carrier phase information recovery (top) and without it (bottom). Notably, the SEB difference between the two scenarios is almost negligible. Conversely, Fig. 5 reports the SEB for $\beta = 3.6$. Given that the values are considerably higher, this suggests that, as expected, the recovery of carrier phase information has a minimal effect on the SEB. Instead, the performance is primarily influenced by the SNR, as a more favorable γ_g configuration (i.e., a lower β) helps mitigate the effects of synchronization errors on estimation accuracy.

C. RESULTS FOR MLE LOCALIZATION

1) CONFIGURATION

Among the metrics for performance evaluation of the localization system, the empirical cumulative density function (ECDF) through Monte Carlo simulations is chosen. The ECDF is computed as follows

$$\mathrm{CDF}(e_{\mathrm{th}}) = \frac{1}{N_{\mathrm{mc}}} \sum_{l=1}^{N_{\mathrm{mc}}} \mathbf{1}(e_l \leq e_{\mathrm{th}}), \tag{66}$$

is the threshold for the localization error, N_{mc} is the number of Monte Carlo simulation and $\mathbf{1}(\cdot)$ is equal to 1 if its logical argument is true, otherwise it is 0, and

$$e_l = ||\hat{\mathbf{p}}_l - \mathbf{p}_{\mathrm{T},l}||$$

where e_l is the localization error, $\mathbf{p}_{\mathrm{T},l}$ and $\hat{\mathbf{p}}_l$ are the true and the estimated position using the MLE algorithm at the lth Monte Carlo run, respectively. In the following, we account for $\beta = 2.6$, $N_{\mathrm{mc}} = 5000$, and for the recovery of the phase information on the carrier frequency. Regarding the MLE, we performed a brute-force search across a $100 \times 100\,\mathrm{m}^2$ region at the center of the overall area, which we assume contains the transmitter. For each Monte Carlo run, the true target position is generated according to a uniform distribution within the search area.

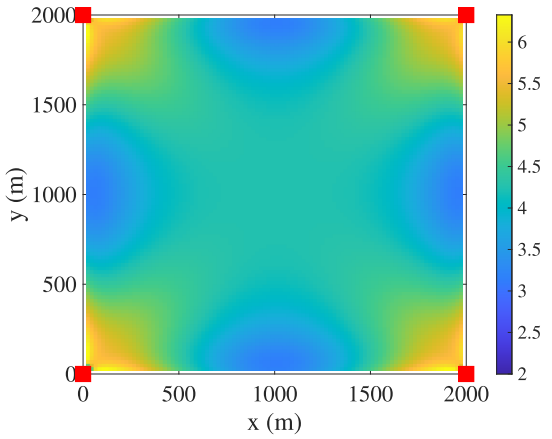

FIGURE 5. SEB in radians obtained for $\beta = 3.6$ and without carrier phase information. Note that, for the sake of readability, the scale is kept different from that of Fig. 4.

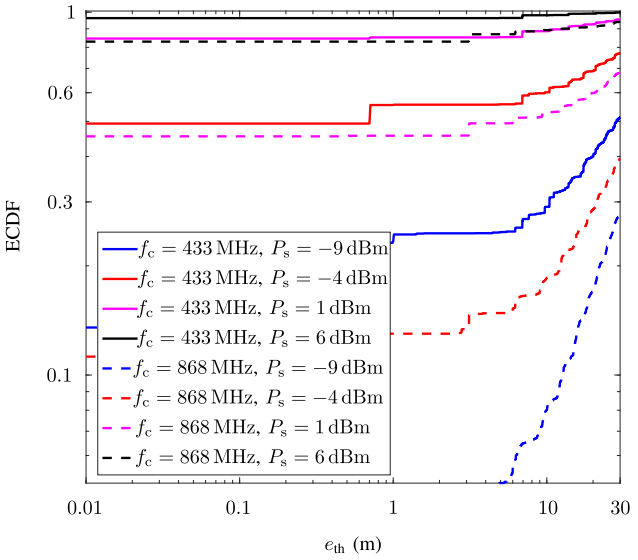

FIGURE 6. ECDF for different values of f_c and P_s, with $\xi = 0$.

2) RESULTS

Figure 6 reports the ECDF for various localization errors when both the central frequency f_c and the transmitted power P_s are adjusted. Continuous lines refer to performance achieved for $f_c = 433\,\mathrm{MHz}$, whereas dashed lines refer to their counterpart achieved for $f_c = 868\,\mathrm{MHz}$. Reducing f_c from 868 MHz to 433 MHz leads to a notable improvement in localization performance. This improvement arises because the decrease in path-loss has a more substantial impact on performance than the slight decrease in accuracy due to the larger wavelength associated with the lower frequency. In other words, the benefit of reduced path-loss at 433 MHz outweighs the potential accuracy loss stemming from the increased wavelength, which slightly reduces spatial resolution.

It is also important to observe that, unlike the PEB, the MLE performance at lower transmission powers, specifically $P_s = -9\,\mathrm{dBm}$, is marked by significantly larger localization errors. For instance, when $f_c = 868\,\mathrm{MHz}$, only about 30% of cases achieve a localization error of less than 30 m, whereas with $f_c = 433\,\mathrm{MHz}$, approximately 40% of cases meet this error threshold. This discrepancy highlights the challenges in solving the ambiguities, especially at higher frequencies where localization is more susceptible to path-loss effects, which are amplified by lower transmission powers. Moreover, large localization errors are observed even when P_s is increased, resulting in higher values of γ_g. This trend can be attributed to the phase periodicity inherent in the system, which introduces ambiguities in the likelihood function. These ambiguities make the system extremely sensitive to noise, thereby necessitating significantly larger values of P_s to mitigate noise effects. Consequently, localization accuracy remains challenged by this effect.

To address these limitations, we evaluated the impact of increasing the number of gateways N_g. Specifically, with $N_g = 8$, localization performance shows considerable improvement. Indeed, the presence of additional gateways

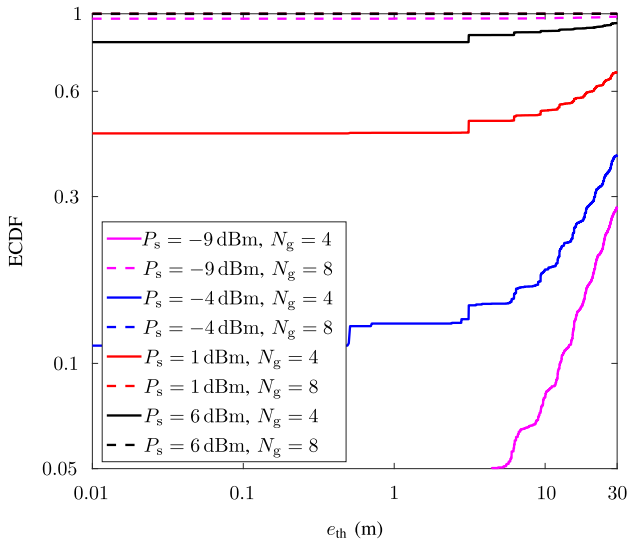

FIGURE 7. ECDF for $f_c = 868$ MHz, different values of P_s, and $\xi = 0$.

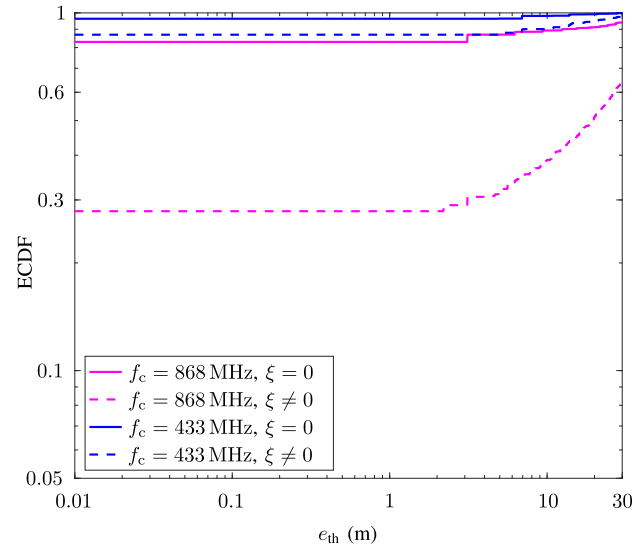

FIGURE 8. ECDF for different values of f_c and under phase synchronization offset. Results are obtained for $P_s = 6$ dBm and SF = 3.

enhances spatial diversity, providing more robust signal measurements that help resolve phase ambiguities and reduce sensitivity to noise. As illustrated by the dotted lines in Fig. 7, this setup with a higher number of gateways leads to more accurate localization results, demonstrating that increasing N_g is an effective strategy to overcome the performance degradation seen at lower P_s and higher f_c values.

Finally, Fig. 8 presents the ECDF for localization errors in scenarios with and without the presence of a phase offset ξ, which is randomly selected for each Monte Carlo cycle, with $\xi \sim \mathcal{U}[0, 2\pi[$. Notably, unlike in the PEB analysis where the impact of ξ was negligible, the inclusion of a phase offset ξ here introduces significant ambiguities in the likelihood function. These ambiguities lead to larger localization errors, as the phase offset complicates the estimation process and increases the likelihood of incorrect localization results (additional computational complexity due to 3D search).

Note that the influence of the phase offset ξ becomes more pronounced when the system operates at lower values of γ_g, which occur at higher values of f_c. When f_c is high, the path-loss increases and γ_g decreases, making the system more susceptible to noise and phase ambiguities introduced by ξ. As a result, the presence of a phase offset has a detrimental effect on localization accuracy since the ambiguities are increased, emphasizing the need for careful handling of ξ when the operating frequency f_c assumes a larger value. Thus, the results in Fig. 8 underscore the importance of managing phase offsets to mitigate their impact on performance, especially when f_c and ξ combine to create more pronounced ambiguities in the likelihood function that can have a detrimental impact for lower γ_g values.

VI. CONCLUSION AND FUTURE PERSPECTIVES

This paper addressed the localization problem in a wireless system with a transmitting LoRa device and multiple gateways serving as anchor nodes. In such settings, we explored the fundamental localization limits, in terms of PEB, for a direct approach that estimates the transmitter's position directly from the received signal, and a two-step TDOA-based approach, which avoids synchronization issues. In both case, we put in evidence the interaction between LoRa signaling and system geometry. Then, we presented the MLE for the direct approach in order to corroborate the previous findings using a localization practical algorithm. Numerical results showed that MLE performance approaches the PEB only at very high SNR regimes, with performance influenced by factors such as the central frequency f_c, phase offset ξ, and the number of gateways N_g. Based on the achieved results, LoRa-based wireless system shows great potential as a promising low-cost and long-range technology for localization purposes for the next generation of wireless systems.

Looking ahead, an important future direction is the extension of the proposed CRLB framework to 3D scenarios. While this extension is mathematically straightforward, since the FIM simply includes an additional coordinate and the derivatives generalize accordingly, it raises several new challenges. In particular, gateway deployment in the vertical dimension and antenna orientation become critical design factors. Moreover, multipath effects are typically more pronounced in 3D environments and should be properly accounted for to achieve reliable localization performance. Finally, in the context of future aerial gateways or drone networks for localization [65], future research could investigate how integrating LoRa technology with such infrastructures may enhance 3D localization performance.

ACKNOWLEDGMENT

The authors would like to thank Marco Chiani for his valuable suggestions and fruitful discussions.

APPENDIX A
FIM ELEMENTS FOR THE DIRECT APPROACH

To compute the FIMs in (25), (26) and (30) on user position, one can operate as follows

$$[\mathbf{J}_g]_{1,1} = \frac{2}{\sigma^2}\sum_{k=0}^{M-1}\Re\left\{\frac{\partial}{\partial x}y_{g,k}\left(\frac{\partial}{\partial x}y_{g,k}\right)^{\star}\right\}, \tag{67}$$

$$[\mathbf{J}_g]_{2,2} = \frac{2}{\sigma^2}\sum_{k=0}^{M-1}\Re\left\{\frac{\partial}{\partial y}y_{g,k}\left(\frac{\partial}{\partial y}y_{g,k}\right)^{\star}\right\}, \tag{68}$$

$$[\mathbf{J}_g]_{1,2} = \frac{2}{\sigma^2}\sum_{k=0}^{M-1}\Re\left\{\frac{\partial}{\partial x}y_{g,k}\left(\frac{\partial}{\partial y}y_{g,k}\right)^{\star}\right\}. \tag{69}$$

Let us focus on the x-coordinate of the user position for now, as the same considerations would also apply to the y-coordinate. The first derivatives of the useful signal $y_{g,k}$ with respect to x is

$$\frac{\partial}{\partial x}y_{g,k} = \left[\frac{\partial}{\partial x}\,\rho_g\right]s_{g,k} + \rho_g\left[\frac{\partial}{\partial x}s_{g,k}\right], \tag{70}$$

where

$$\frac{\partial}{\partial x}\rho_g = \frac{\partial}{\partial x}\left(\frac{\kappa}{f_c^2 d_g^{\beta}}\right)^{\frac{1}{2}} = -\frac{\beta}{2}\frac{\rho_g}{d_g}\frac{x-x_g}{d_g}, \tag{71}$$

$$\frac{\partial}{\partial x}s_{g,k} = j\,s_{g,k}\,\frac{2\pi B}{M\,c}\frac{\partial d_g}{\partial x}\left[\frac{M}{2} + B\tau_g - k - M\frac{f_c}{B}\right]. \tag{72}$$

By substituting (71) and (72) into (70), we can write

$$\frac{\partial}{\partial x}y_{g,k} = y_{g,k}\frac{(x-x_g)}{d_g^2}\left[-\frac{\beta}{2} + jd_g A_{g,k}^{(1)}\right], \tag{73}$$

where $A_{g,k}^{(1)}$ is defined as in (23). Analogously to (73), we can compute the first derivative of $y_{g,k}$ with respect to y as

$$\frac{\partial}{\partial y}y_{g,k} = y_{g,k}\frac{(y-y_g)}{d_g^2}\left[-\frac{\beta}{2} + jd_g A_{g,k}^{(1)}\right]. \tag{74}$$

By substituting (73) in (67),we obtain

$$\begin{aligned}[\mathbf{J}_g]_{1,1} &= \frac{2}{\sigma^2}\sum_{k=0}^{M-1}\Re\left\{\frac{\partial}{\partial x}y_{g,k}\left(\frac{\partial}{\partial x}y_{g,k}\right)^{\star}\right\}\\ &= \frac{2}{\sigma^2}\frac{(x-x_g)^2}{d_g^4}\sum_{k=0}^{M-1}|y_{g,k}|^2\cdot\left|-\frac{\beta}{2} + j\,d_g\,A_{g,k}^{(1)}\right|^2\\ &= \frac{2\,P_s\rho_g^2}{\sigma^2}\,\Gamma_g\,\frac{(x-x_g)^2}{d_g^4},\end{aligned} \tag{75}$$

where

$$\begin{aligned}\Gamma_g &= \sum_{k=0}^{M-1}\left|-\frac{\beta}{2} + j\,d_g\,A_{g,k}^{(1)}\right|^2\\ &= \frac{M\beta^2}{4} + d_g^2\sum_{k=0}^{M-1}\left(A_{g,k}^{(1)}\right)^2.\end{aligned} \tag{76}$$

Now, recalling that

$$A_{g,k}^{(1)} = \frac{B\pi}{Mc}\left[M + 2B\tau_g - 2\,k - 2M\frac{f_c}{B}\right], \tag{77}$$

which quantifies how the received phase changes with the propagation time, let us focus on the second term of (76)

$$\begin{aligned}\sum_{k=0}^{M-1}\left(A_{g,k}^{(1)}\right)^2 &= \frac{B^2\pi^2}{M^2\,c^2}\sum_{k=0}^{M-1}\left[\tilde{A}_g - 2\,k\right]^2\\ &= \frac{B^2\pi^2}{M^2\,c^2}\sum_{k=0}^{M-1}\left[\tilde{A}_g^2 + 4\,k^2 - 4\,k\,\tilde{A}_g\right]\\ &= \frac{B^2\pi^2}{M^2c^2}\left(M\tilde{A}_g^2 + 4\sum_{k=0}^{M-1}k^2 - 4\tilde{A}_g\sum_{k=0}^{M-1}k\right),\end{aligned}$$

which finally gives

$$\begin{aligned}\sum_{k=0}^{M-1}\left(A_{g,k}^{(1)}\right)^2 = \frac{B^2\pi^2}{Mc^2}\Bigg[M^2\left(\frac{1}{3} + \frac{4f_c^2}{B^2}\right) - M\left(\frac{4f_c}{B} - 8f_c\,\tau_g\right)\\ + \left(\frac{2}{3} + 4B^2\,\tau_g^2 + 4B\,\tau_g\right)\Bigg],\end{aligned} \tag{78}$$

with $\tilde{A}_g = \left(M + 2B\tau_g - 2M\frac{f_c}{B}\right)$. Consequently, we can write Γ_g in (76) as

$$\Gamma_g = \frac{M\beta^2}{4} + d_g^2\sum_{k=0}^{M-1}\left(A_{g,k}^{(1)}\right)^2, \tag{79}$$

$$\begin{aligned}&= \frac{M\beta^2}{4} + \frac{(\tau_g B\pi)^2}{M}\\ &\quad\times\left[M^2\left(\frac{1}{3} + \frac{4f_c^2}{B^2}\right) + -M\left(\frac{4f_c}{B} - 8f_c\,\tau_g\right)\right.\\ &\quad\left.+\left(\frac{2}{3} + 4B^2\,\tau_g^2 + 4B\,\tau_g\right)\right].\end{aligned} \tag{80}$$

The same holds for the FIM on the y-coordinate (26) and on the cross term (30).

Regarding the FIM that depends on the initial synchronization phase, it is easy to show that

$$\begin{aligned}[\mathbf{J}_g]_{3,3} &= \frac{2}{\sigma^2}\sum_{k=0}^{M-1}\Re\left\{\frac{\partial\,y_{g,k}}{\partial\xi}\left(\frac{\partial\,y_{g,k}}{\partial\xi}\right)^{\star}\right\}\\ &= \frac{2}{\sigma^2}\sum_{k=0}^{M-1}|y_{g,k}|^2 = \frac{2\,MP_s\,\rho_g^2}{\sigma^2}.\end{aligned} \tag{81}$$

The cross-terms in (31)-(32) can be found as

$$\begin{aligned}[\mathbf{J}_g]_{1,3} &= \frac{2}{\sigma^2}\sum_{k=0}^{M-1}\Re\left\{\frac{\partial\,y_{g,k}}{\partial x}\left(\frac{\partial\,y_{g,k}}{\partial\xi}\right)^{\star}\right\}\\ &= \frac{2}{\sigma^2}\sum_{k=0}^{M-1}\Re\left\{y_{g,k}\left(-\frac{\beta}{2} + jd_g A_{g,k}^{(1)}\right)\left(\frac{x-x_g}{d_g^2}\right)\left(-jy_{g,k}^{\star}\right)\right\}\\ &= \frac{2\,P_s\,\rho_g^2}{\sigma^2}\left(\frac{x-x_g}{d_g^2}\right)\sum_{k=0}^{M-1}\Re\left\{j\,\frac{\beta}{2} + d_g\,A_{g,k}^{(1)}\right\}\\ &= \frac{2\,P_s\,\rho_g^2}{\sigma^2}\left(\frac{x-x_g}{d_g}\right)\sum_{k=0}^{M-1}A_{g,k}^{(1)}.\end{aligned} \tag{82}$$

Now consider the following summation

$$\Omega_g = \sum_{k=0}^{M-1} A_{g,k}^{(1)} = \frac{B\pi}{c}\left(M + 2B\tau_g - 2M\frac{f_c}{B}\right) - \frac{2B\pi}{Mc}\sum_{k=0}^{M-1} k = \frac{2\,\pi\,\tau_g\,B^2 + \pi\,B - 2\,M\,f_c\,\pi}{c}. \tag{83}$$

By substituting (83) in (82) it is possible to obtain (31). The same computations can be done to obtain (32).

APPENDIX B
FIM ELEMENTS FOR DELAY ESTIMATION

To compute the FIM in (59) we need to consider the following first derivative of $y_{g,k}$ with respect to τ_g

$$\frac{\partial}{\partial \tau_g} y_{g,k} = s_{g,k} \cdot \frac{\partial \rho_g}{\partial \tau_g} + \rho_g \cdot \frac{\partial s_{g,k}}{\partial \tau_g}, \tag{84}$$

where

$$\frac{\partial \rho_g}{\partial \tau_g} = \frac{\partial}{\partial \tau_g}\left(\frac{\kappa\, c^{\beta}}{f_c^2 \tau_g^{\beta}}\right)^{\frac{1}{2}} = -\frac{\beta \rho_g}{2\tau_g}. \tag{85}$$

Thus, regarding the first term of (84) we have

$$s_{g,k}\frac{\partial \rho_g}{\partial \tau_g} = -\frac{\beta}{2\tau_g} y_{g,k}. \tag{86}$$

Then, considering the term $\frac{\partial s_{g,k}}{\partial \tau_g}$ in (84), we can write

$$\frac{\partial s_{g,k}}{\partial \tau_g} = s_{g,k}\left[j2\pi \frac{-2\,k\,B^2\,T + 2B^2\tau_g + MB - 2Mf_c}{2M}\right] = j\,2\,\pi\, s_{g,k}\, A_{g,k}^{(2)}, \tag{87}$$

Then, by substituting (85) and (87) into (84), we can write

$$\frac{\partial y_{g,k}}{\partial \tau_g} = y_{g,k}\Big[-\frac{\beta}{2\tau_g} + j\,2\pi A_{g,k}^{(2)}\Big], \tag{88}$$

and by considering that

$$\sum_{k=0}^{M-1}\left(A_{g,k}^{(2)}\right)^2 = \frac{1}{12M}\cdot\Big(12B^4\,\tau_g^2 + 12B^3\tau_g + B^2M^2 - 24B^2Mf_c\tau_g + 2B^2 - 12BMf_c + 12M^2f_c^2\Big), \tag{89}$$

so that it possible to obtain (65).

REFERENCES

[1] Q. Zhou, K. Zheng, L. Hou, J. Xing, and R. Xu, "Design and implementation of open LoRa for IoT," *IEEE Access*, vol. 7, pp. 100649–100657, 2019.

[2] C. Anton-Haro and M. Dohler, *Machine-to-Machine (M2M) Communications: Architecture, Performance and Applications*. Amsterdam, The Netherlands: Elsevier, 2014.

[3] S. Li, L. D. Xu, and S. Zhao, "The Internet of Things: A survey," *Comput. Netw.*, vol. 17, no. 2, pp. 243–259, 2014.

[4] J. Gubbi, R. Buyya, S. Marusic, and M. Palaniswami, "Internet of Things (IoT): A vision, architectural elements, and future directions," *Future Gener. Comput. Syst.*, vol. 29, no. 7, pp. 1645–1660, Sep. 2013.

[5] D. Miorandi, S. Sicari, F. De Pellegrini, and I. Chlamtac, "Internet of Things: Vision, applications and research challenges," *Ad Hoc Netw.*, vol. 10, no. 7, pp. 1497–1516, Sep. 2012.

[6] A. Raychowdhury and A. Pramanik, "Survey on LoRa technology: Solution for Internet of Things," in *Intelligent Systems, Technologies and Applications*, S. M. Thampi, L. Trajkovic, S. Mitra, P. Nagabhushan, El-S. M. El-Alfy, Z. Bojkovic, and D. Mishra, Eds., Singapore: Springer, 2020, pp. 259–271.

[7] R. Marini, K. Mikhaylov, G. Pasolini, and C. Buratti, "Low-power wide-area networks: Comparison of LoRaWAN and NB-IoT performance," *IEEE Internet Things J.*, vol. 9, no. 21, pp. 21051–21063, Nov. 2022.

[8] U. Noreen, A. Bounceur, and L. Clavier, "A study of LoRa low power and wide area network technology," in *Proc. Int. Conf. Adv. Technol. Signal Image Process. (ATSIP)*, May 2017, pp. 1–6.

[9] D. Wang, A. Elzanaty, and M.-S. Alouini, "Coded frequency hopping for direct-to-satellite IoT systems: Design and analysis," *IEEE Internet Things J.*, vol. 11, no. 22, pp. 36335–36349, Nov. 2024.

[10] M. Chiani and A. Elzanaty, "On the LoRa modulation for IoT: Waveform properties and spectral analysis," *IEEE Internet Things J.*, vol. 6, no. 5, pp. 8463–8470, Oct. 2019.

[11] G. Pasolini, "On the LoRa chirp spread spectrum modulation: Signal properties and their impact on transmitter and receiver architectures," *IEEE Trans. Wireless Commun.*, vol. 21, no. 1, pp. 357–369, Jan. 2022.

[12] A. W. Azim, R. Shubair, and M. Chafii, "Chirp spread spectrum-based waveform design and detection mechanisms for LPWAN-based IoT: A survey," *IEEE Access*, vol. 12, pp. 24949–25017, 2024.

[13] C. Demeslay, P. Rostaing, and R. Gautier, "Theoretical performance of LoRa system in multipath and interference channels," *IEEE Internet Things J.*, vol. 9, no. 9, pp. 6830–6843, May 2022.

[14] H. Ma, G. Cai, Y. Fang, P. Chen, and G. Han, "Design and performance analysis of a new STBC-MIMO LoRa system," *IEEE Trans. Commun.*, vol. 69, no. 9, pp. 5744–5757, Sep. 2021.

[15] X. Zhang, W. Xu, G. Cai, Y. Song, and G. Chen, "A new reconfigurable intelligent-surface-assisted LoRa system," *IEEE Trans. Veh. Technol.*, vol. 71, no. 8, pp. 9055–9060, Aug. 2022.

[16] G. Lin, A. Elzanaty, and M.-S. Alouini, "LoRa backscatter communications: Temporal, spectral, and error performance analysis," *IEEE Internet Things J.*, vol. 10, no. 18, pp. 16412–16426, Sep. 2023.

[17] L. Bariah, W. Jaafar, S. Muhaidat, H. Elgala, and H. Yanikomeroglu, "On the error performance of LoRa-enabled aerial networks over shadowed Rician fading channels," *IEEE Commun. Lett.*, vol. 26, no. 10, pp. 2322–2326, Oct. 2022.

[18] M. A. Ullah, G. Pasolini, K. Mikhaylov, and H. Alves, "Understanding the limits of LoRa direct-to-satellite: The Doppler perspectives," *IEEE Open J. Commun. Soc.*, vol. 5, pp. 51–63, 2024.

[19] T. H. Nguyen, W.-S. Jung, L. T. Tu, T. V. Chien, D. Yoo, and S. Ro, "Performance analysis and optimization of the coverage probability in dual hop LoRa networks with different fading channels," *IEEE Access*, vol. 8, pp. 107087–107102, 2020.

[20] H. Zhang, G. Liu, Y. Xu, and T. Jiang, "LoRaAid: Underground joint communication and localization system based on LoRa technology," *IEEE Trans. Wireless Commun.*, vol. 23, no. 5, pp. 5248–5260, May 2024.

[21] Z. Song, S. Tong, and J. Wang, "LoSense: Integrated long-range sensing and communication with LoRa signals," in *Proc. IEEE 31st Int. Conf. Netw. Protocols (ICNP)*, Oct. 2023, pp. 1–11.

[22] M. Z. Win, A. Conti, S. Mazuelas, Y. Shen, W. M. Gifford, D. Dardari, and M. Chiani, "Network localization and navigation via cooperation," *IEEE Commun. Mag.*, vol. 49, no. 5, pp. 56–62, May 2011.

[23] R. M. Buehrer, H. Wymeersch, and R. M. Vaghefi, "Collaborative sensor network localization: Algorithms and practical issues," *Proc. IEEE*, vol. 106, no. 6, pp. 1089–1114, Jun. 2018.

[24] A. Guerra, F. Guidi, and D. Dardari, "On the impact of beamforming strategy on mm-wave localization performance limits," in *Proc. IEEE Int. Conf. Commun. Workshops (ICC Workshops)*, May 2017, pp. 809–814.

[25] A. Conti, S. Mazuelas, S. Bartoletti, W. C. Lindsey, and M. Z. Win, "Soft information for Localization-of-Things," *Proc. IEEE*, vol. 107, no. 11, pp. 2240–2264, Nov. 2019.

[26] K. Witrisal, P. Meissner, E. Leitinger, Y. Shen, C. Gustafson, F. Tufvesson, K. Haneda, D. Dardari, A. F. Molisch, A. Conti, and M. Z. Win, "High-accuracy localization for assisted living: 5G systems will turn multipath channels from foe to friend," *IEEE Signal Process. Mag.*, vol. 33, no. 2, pp. 59–70, Mar. 2016.

[27] M. Chiani, A. Giorgetti, and E. Paolini, "Sensor radar for object tracking," *Proc. IEEE*, vol. 106, no. 6, pp. 1022–1041, Jun. 2018.

[28] A. Guerra, F. Guidi, J. Dall'Ara, and D. Dardari, "Occupancy grid mapping for personal radar applications," in *Proc. IEEE Stat. Signal Process. Workshop (SSP)*, Jun. 2018, pp. 766–770.
[29] L. E. Marquez and M. Calle, "Understanding LoRa-based localization: Foundations and challenges," *IEEE Internet Things J.*, vol. 10, no. 13, pp. 11185–11198, Jul. 2023.
[30] C. Gu, L. Jiang, and R. Tan, "LoRa-based localization: Opportunities and challenges," in *Proc. Int. Conf. Embedded Wireless Syst. Netw.*, Oct. 2019, pp. 413–418.
[31] K. Kim, S. Li, M. Heydariaan, N. Smaoui, O. Gnawali, W. Suh, M. J. Suh, and J. I. Kim, "Feasibility of LoRa for smart home indoor localization," *Appl. Sci.*, vol. 11, no. 1, p. 415, Jan. 2021.
[32] T. J. Ng, N. Kumar, and M. Othman, "LoRa-based indoor positioning in dynamic industrial environments using deep Gaussian process regression and temporal-based enhancements," *IEEE Access*, vol. 12, pp. 165298–165313, 2024.
[33] Y. Lin, W. Dong, Y. Gao, and T. Gu, "SateLoc: A virtual fingerprinting approach to outdoor LoRa localization using satellite images," *ACM Trans. Sensor Netw.*, vol. 17, no. 4, pp. 1–28, Nov. 2021.
[34] A. Lazaro, M. Lazaro, and R. Villarino, "Room-level localization system based on LoRa backscatters," *IEEE Access*, vol. 9, pp. 16004–16018, 2021.
[35] A. Mackey and P. Spachos, "LoRa-based localization system for emergency services in GPS-less environments," in *Proc. IEEE Conf. Comput. Commun. Workshops*, Apr. 2019, pp. 939–944.
[36] E. Goldoni, L. Prando, A. Vizziello, P. Savazzi, and P. Gamba, "Experimental data set analysis of RSSI-based indoor and outdoor localization in LoRa networks," *Internet Technol. Lett.*, vol. 2, no. 1, p. 75, Jan. 2019.
[37] K.-H. Lam, C.-C. Cheung, and W.-C. Lee, "LoRa-based localization systems for noisy outdoor environment," in *Proc. IEEE 13th Int. Conf. Wireless Mobile Comput., Netw. Commun. (WiMob)*, Oct. 2017, pp. 278–284.
[38] K.-H. Lam, C.-C. Cheung, and W.-C. Lee, "New RSSI-based LoRa localization algorithms for very noisy outdoor environment," in *Proc. IEEE 42nd Annu. Comput. Softw. Appl. Conf. (COMPSAC)*, vol. 2, Jul. 2018, pp. 794–799.
[39] K.-H. Lam, C.-C. Cheung, and W.-C. Lee, "RSSI-based LoRa localization systems for large-scale indoor and outdoor environments," *IEEE Trans. Veh. Technol.*, vol. 68, no. 12, pp. 11778–11791, Dec. 2019.
[40] H. Chen, F. Xing, Q. Yang, Y. Shu, Z. Shi, J. Chen, and Z. Tao, "A lightweight mobile-anchor-based multi-target outdoor localization scheme using LoRa communication," *IEEE Trans. Green Commun. Netw.*, vol. 7, no. 4, pp. 1607–1619, Dec. 2023.
[41] V. Delafontaine, F. Schiano, G. Cocco, A. Rusu, and D. Floreano, "Drone-aided localization in LoRa IoT networks," in *Proc. IEEE Int. Conf. Robot. Autom. (ICRA)*, May 2020, pp. 286–292.
[42] K. Hirotsu, F. Granelli, and A. Nakao, "LoRa-based localization for drones: Methodological enhancements explored through simulations and real-world experiments," *IEEE Access*, vol. 12, pp. 145988–145996, 2024.
[43] W.-J. Shin, Y. Lee, J. Cho, J. Jang, Y. Seo, and S. Kahng, "RSSI improved for LoRa wireless communication, field-tested in the wide-open area," *IEEE Access*, vol. 11, pp. 80172–80180, 2023.
[44] M. S. Yahya, S. Soeung, S. K. A. Rahim, T. K. Geok, and U. Musa, "Machine learning-optimized wearable antenna for LoRa localization," *IEEE Access*, vol. 12, pp. 139237–139252, 2024.
[45] E. H. Yoshitome, J. V. R. da Cruz, M. E. P. Monteiro, and J. L. Rebelatto, "LoRa-aided outdoor localization system: RSSI or TDoA?" *Internet Technol. Lett.*, vol. 5, no. 2, pp. 1–10, Mar. 2022.
[46] F. Adelantado, X. Vilajosana, P. Tuset-Peiro, B. Martinez, J. Melia-Segui, and T. Watteyne, "Understanding the limits of LoRaWAN," *IEEE Commun. Mag.*, vol. 55, no. 9, pp. 34–40, Sep. 2017.
[47] D. F. Carvalho, A. Depari, P. Ferrari, A. Flammini, S. Rinaldi, and E. Sisinni, "On the feasibility of mobile sensing and tracking applications based on LPWAN," in *Proc. IEEE Sensors Appl. Symp. (SAS)*, Mar. 2018, pp. 1–6.
[48] Y. Qi and H. Kobayashi, "On relation among time delay and signal strength based geolocation methods," in *Proc. IEEE Global Telecommun. Conf.*, Jun. 2003, pp. 4079–4083.
[49] H. Kremo, T. Farrell, J. Tallon, D. McDonald, and L. Doyle, "A method to enhance ranging resolution for localization of LoRa sensors," in *Proc. IEEE 28th Annu. Int. Symp. Pers., Indoor, Mobile Radio Commun. (PIMRC)*, Oct. 2017, pp. 1–6.
[50] B. C. Fargas and M. N. Petersen, "GPS-free geolocation using LoRa in low-power WANs," in *Proc. Global Internet Things Summit (GIoTS)*, Jun. 2017, pp. 1–6.
[51] N. Podevijn, D. Plets, J. Trogh, L. Martens, P. Suanet, K. Hendrikse, and W. Joseph, "TDoA-based outdoor positioning with tracking algorithm in a public LoRa network," *Wireless Commun. Mobile Comput.*, vol. 2018, no. 1, pp. 1–12, Jan. 2018.
[52] J. Liu, J. Gao, S. Jha, and W. Hu, "Seirios: Leveraging multiple channels for LoRaWAN indoor and outdoor localization," in *Proc. 27th Annu. Int. Conf. Mobile Comput. Netw.*, Oct. 2021, pp. 656–669.
[53] C. Gu, L. Jiang, and R. Tan, "LoRa-based localization: Opportunities and challenges," 2018, *arXiv:1812.11481*.
[54] T. Farrell, H. Kremo, and J. Tallon, "System and method to enhance ranging resolution for localization of a LoRa sensor or device," U.S. Patent 11 026 192, Jun. 1, 2021.
[55] Y. Han, Y. Shen, X.-P. Zhang, M. Z. Win, and H. Meng, "Performance limits and geometric properties of array localization," *IEEE Trans. Inf. Theory*, vol. 62, no. 2, pp. 1054–1075, Feb. 2016.
[56] Y. Shen and M. Z. Win, "Fundamental limits of wideband localization—Part I: A general framework," *IEEE Trans. Inf. Theory*, vol. 56, no. 10, pp. 4956–4980, Oct. 2010.
[57] H. Godrich, A. M. Haimovich, and R. S. Blum, "Cramer Rao bound on target localization estimation in MIMO radar systems," in *Proc. 42nd Annu. Conf. Inf. Sci. Syst.*, Mar. 2008, pp. 134–139.
[58] A. Guerra, F. Guidi, and D. Dardari, "Single-anchor localization and orientation performance limits using massive arrays: MIMO vs. beamforming," *IEEE Trans. Wireless Commun.*, vol. 17, no. 8, pp. 5241–5255, Aug. 2018.
[59] A. Shahmansoori, G. E. Garcia, G. Destino, G. Seco-Granados, and H. Wymeersch, "Position and orientation estimation through millimeter-wave MIMO in 5G systems," *IEEE Trans. Wireless Commun.*, vol. 17, no. 3, pp. 1822–1835, Mar. 2018.
[60] H. Linka, M. Rademacher, O. G. Aliu, and K. Jonas, *Path Loss Models for Low-power Wide-area Networks: Experimental Results Using LoRa*. Berlin, Germany: VDE Verlag, 2018.
[61] H. Godrich, A. P. Petropulu, and H. V. Poor, "Power allocation strategies for target localization in distributed multiple-radar architectures," *IEEE Trans. Signal Process.*, vol. 59, no. 7, pp. 3226–3240, Jul. 2011.
[62] S. M. Kay, *Fundamentals of Statistical Signal Processing: Estimation Theory*. Upper Saddle River, NJ, USA: Prentice-Hall, 1993.
[63] H. Chen, H. Sarieddeen, T. Ballal, H. Wymeersch, M.-S. Alouini, and T. Y. Al-Naffouri, "A tutorial on terahertz-band localization for 6G communication systems," *IEEE Commun. Surveys Tuts.*, vol. 24, no. 3, pp. 1780–1815, 3rd Quart., 2022.
[64] D. Dardari, A. Conti, U. Ferner, A. Giorgetti, and M. Z. Win, "Ranging with ultrawide bandwidth signals in multipath environments," *Proc. IEEE*, vol. 97, no. 2, pp. 404–426, Feb. 2009.
[65] A. Guerra, F. Guidi, D. Dardari, and P. M. Djuric, "Networks of UAVs of low complexity for time-critical localization," *IEEE Aerosp. Electron. Syst. Mag.*, vol. 37, no. 10, pp. 22–38, Oct. 2022.

AMIR SHEHNI (Member, IEEE) received the B.Sc. degree in electrical engineering (power) from Azad University, Najafabad, Iran, in 2007, the M.Sc. degree in electrical engineering (radio communications) from the Blekinge Institute of Technology (BTH), Karlskrona, Sweden, with thesis work at Chalmers University of Technology, Gothenburg, Sweden, in 2013, and the Ph.D. degree in electronic engineering from University College Dublin (UCD), Dublin, Ireland, in 2019. He has held Postdoctoral Research positions at the National Research Council of Italy (CNR-IEIIT) and the University of Bologna, Italy, from 2022 to 2024, and at Humboldt University of Berlin, Germany, since 2024. He also has several years of industry experience with Agahan Company, Pars Ghodrat Company, and iris GmbH. His research interests include wireless communications, localization and positioning, signal and image processing, and computer vision.

AHMED ELZANATY (Senior Member, IEEE) received the Ph.D. degree in electronics, telecommunications, and information technology from the University of Bologna, Italy, in 2018. Currently, he is a Lecturer (an Assistant Professor) with the Institute for Communication Systems, University of Surrey, U.K. He is serving as the Secretary of the Radio Communications Committee (RCC), IEEE Communications Society. He has participated in several national and European projects, such as TUDOR, CHEDDAR, and EuroCPS. His research interests include the design and performance analysis of wireless communication and localization systems.

FRANCESCO GUIDI (Member, IEEE) received the M.S. degree (summa cum laude) in electronics and telecommunications engineering from the University of Bologna, Italy, in 2009, and the joint Ph.D. degree in information engineering from the École Polytechnique, Paris, France, and the University of Bologna, in 2013. He is currently a Senior Researcher with the National Research Council of Italy (CNR), Institute of Electronics, Computer, and Telecommunication Engineering (IEIIT). From 2015 to 2017, he held a research position funded by an individual European Marie-Curie Fellowship at French Alternative Energies and Atomic Energy Commission (CEA), LETI, Grenoble, France. He received the IEEE Marconi Prize Paper Award in Wireless Communications, in 2025; the Best Student Paper Award at the International Conference on UltrawideBand, Paris, France, in 2014; and the Best Paper Award at the International Conference on Autonomous Systems, Montreal, Canada, in 2021. In 2022 and 2023, he was recognized as an Exemplary Reviewer for IEEE COMMUNICATIONS LETTERS. He serves as an Associate Editor for IEEE TRANSACTIONS ON COMMUNICATIONS and IEEE TRANSACTIONS ON MOBILE COMPUTING. He served as an Associated Editor for IEEE WIRELESS COMMUNICATIONS LETTERS, from 2021 to 2025; and a Guest Editor for IEEE INTERNET OF THINGS JOURNAL and IEEE TRANSACTIONS ON AEROSPACE AND ELECTRONIC SYSTEMS, in 2025.

ANNA GUERRA (Member, IEEE) received the Ph.D. degree in electronics, telecommunications, and information technologies from the University of Bologna, in 2016. She has been an Associate Professor with the University of Bologna, since 2024. Previously, she was a Researcher with the National Research Council (CNR) of Italy. From 2016 to 2021, she received the Global Marie Skłodowska-Curie Research Fellowship for the H2020 AirSens Project. She visited Stony Brook University, Stony Brook, NY, USA, as part of this fellowship. In 2023, she received the ERC Starting Grant Fellowship for the CUE-GO Project. Her research interests include radio localization and mapping, smart radio environments, and distributed signal processing for networks of autonomous agents. She received the Best Student Paper Award at IEEE ICUWB 2014 (Paris, France) and the Best Paper Award at IEEE RFID-TA 2019 (Pisa, Italy) and IEEE ICAS 2021 (Montreal, QC, Canada). She is an Associate Editor of IEEE TRANSACTIONS ON WIRELESS COMMUNICATIONS, IEEE COMMUNICATIONS LETTERS, and IEEE WIRELESS COMMUNICATIONS LETTERS.

GIANNI PASOLINI (Member, IEEE) is an Associate Professor with the University of Bologna, Italy. Throughout his career, he has been actively involved in several European initiatives on wireless communications, including COST Actions and Networks of Excellence. His research interests include wireless communication systems, the Internet of Things, digital signal processing, and THz communications. He has been a member of the organizing committee for several IEEE conferences. He is also one of the founding members of the ''National Laboratory of Wireless Communications—WiLab,'' part of the National Inter-University Consortium for Telecommunications, Italy. He serves as an Associate Editor for IEEE OPEN JOURNAL OF THE COMMUNICATIONS SOCIETY.

DAVIDE DARDARI (Fellow, IEEE) is a Full Professor at the University of Bologna, Italy. He has been a Research Affiliate at the Massachusetts Institute of Technology, USA. His interests are in wireless communications, localization techniques, smart radio environments, and distributed signal processing. He received the IEEE Aerospace and Electronic Systems Society's M. Barry Carlton Award (2011), the IEEE Communications Society's Fred W. Ellersick Prize (2012), and the IEEE Marconi Prize Paper Award in Wireless Communications (2025). He was the Chair of the Radio Communications Committee and a Distinguished Lecturer (2018-2019) of the IEEE Communications Society. He served as an Editor for IEEE TRANSACTIONS ON WIRELESS COMMUNICATIONS from 2006 to 2012. Currently, he is a Senior Member of the Editorial Board of the IEEE *Signal Processing Magazine*.